Renewable and Sustainable Energy Reviews 192 (2024) 114206

Contents lists available at ScienceDirect

Renewable and Sustainable Energy Reviews

journal homepage: www.elsevier.com/locate/rser

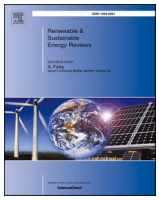

Wave energy conversion by an array of oscillating water columns deployed along a long-flexible floating breakwater

Yong Cheng [a], Weiming Du [a], Saishuai Dai [b,*], Zhiming Yuan [a,b], Atilla Incecik [b]

[a] School of Naval Architecture and Ocean Engineering, Jiangsu University of Science and Technology, Zhenjiang, 212003, China
[b] Naval Architecture, Ocean and Marine Engineering Department, University of Strathclyde, Glasgow, United Kingdom

ARTICLE INFO

Keywords:
Array OWCs
Long-flexible floating breakwater
Wave energy conversion
CFD-FEM hybrid model
Hydroelastic response
Oblique incident wave

ABSTRACT

Large-scale spatial configurations combining Wave Energy Converters (WECs) and coastal attenuating-wave facilities have the potential to exploit marine renewable energy sustainably. In this study, an integrated concept of multiple Oscillating Water Columns (OWCs) and a very long floating breakwater is introduced. Associated energy extraction, gap resonance and hydroelastic interaction problems are examined. A coupled numerical simulation methodology consisting of a Finite Volume Method (FVM)based solver and a Finite Element Method (FEM) solver, is developed to investigate the strong fluid and structure coupled problem. The fluid-structure information is matched in real-time and the flexible modes of the floating breakwater are obtained by imposing a restrained beam inside the pontoon. The accurate time-domain model is validated against both simulated and measured data. Extensive parametric studies indicate that the energy conversion has a conflict with the wave attenuation in terms of determining the along-shore number of OWCs. The highest energy conversion in medium-period and long-period waves are observed in the OWCs near the end and middle locations, respectively. Besides, the constructive resonant gap effect between OWCs and the breakwater can amplify the peaks of energy conversion efficiency, leads to a sudden collapse in transmission coefficient curves. With an increased sidewall draft, OWCs closer to oblique incident direction generate stronger piston-type and sloshing oscillations. Additionally, compared with a rigid breakwater, the elastic deformation of the breakwater plays a destructive role in wave energy conversion, which is attributed to the out-of-phase interference of multi-mode radiated waves.

1. Introduction

Fossil fuels such as coal, oil and natural gas have been used as energy resources to drive the rapid development of human society in the past two centuries. However, the excessive usage of fossil fuels leads to climate-warming problems i.e. global greenhouse effect. According to the global energy review, the International Energy Agency (IEA) estimated that energy-related CO_2 emissions grow to 36.3 Gt in 2021 with a 6% increase compared to the emission level of 2020 [1]. To fight global warming, a transition from fossil fuels to alternative renewable energy resources is inevitable. Renewable energy is becoming more and more competitive in the energy landscape as shown in Fig. 1, which is summarized from the data in Word Energy Transitions Outlook 2022 recorded by the International Renewable Energy Agency (IREA) [2]. Wave energy as one of marine renewable energy, is estimated to have a 2.11 TW potential which is almost 20% of the global energy demand [3]. Consequently, using Wave Energy Converters (WECs) to extract wave energy and then generate electricity is a promising solution to mitigate climate warming. So far, various concepts of WECs have been proposed, which are generally classified into Oscillating Water Column (OWC), Oscillating Buoy (OB) and overtopping converter [4]. Nevertheless, the high deployment cost and the low energy conversion efficiency have hindered the commercialization of WECs compared with other renewable energy, i.e. solar photovoltaic and wind energy [5]. Integrating WECs with other offshore structures would be an effective way to enhance the accessibility of commercial-scale wave energy operations.

Offshore WEC-infrastructure integrated systems include WEC-floating breakwater hybrid system, WEC-Offshore Wind Turbine (OWT) hybrid system, WEC-floating platform hybrid system, and WEC-aquaculture facility hybrid system. There are multiple benefits of these types of offshore integrated systems. Firstly, the total output power per unit ocean spacewill increase due to sharing of ocean space. Chen et al. [6] conducted both numerical and experimental investigations on a

* Corresponding author.
E-mail address: saishuai.dai@strath.ac.uk (S. Dai).

https://doi.org/10.1016/j.rser.2023.114206
Received 10 April 2023; Received in revised form 14 November 2023; Accepted 9 December 2023
Available online 23 December 2023

Nomenclature

Symbols

α	OWC opening ratio [−]
B_b	breakwater width [m]
B_g	distance between OWCs and breakwater [m]
B_o	OWC width [m]
d_b	breakwater draft [m]
d_{o1}	OWC front wall draft [m]
d_{o2}	OWC sidewall draft [m]
EI	bending rigidity [Nm^2]
h	water depth [m]
H_I	incident wave height [m]
L_b	breakwater length [m]
L_o	OWC length [m]
N	the number of OWCs [−]
R	radius of circular orifice [m]
T	wave period [s]

Abbreviations

CV	Control Volume
CFD	Computation Fluid Dynamics
FEM	Finite Element Method
IEA	International Energy Agency
LCOE	Levelized Cost of Energy
LIMPET	Land Installed Marine Powered Energy Transformer
OB	Oscillating buoy
OSPREY	Ocean Swell Powered Renewable Energy
OWC	Oscillating water column
OWT	Offshore wind turbine
PRFB	Pile-constrained floating breakwater
PTO	Power take off
RANS	Reynolds-Averaged Navier-Stokes
TBW	The Berkeley Wedge
URF	Under relaxation factor
VOF	Volume of fluid
WEC	3-D Wave energy converter Three-dimensional

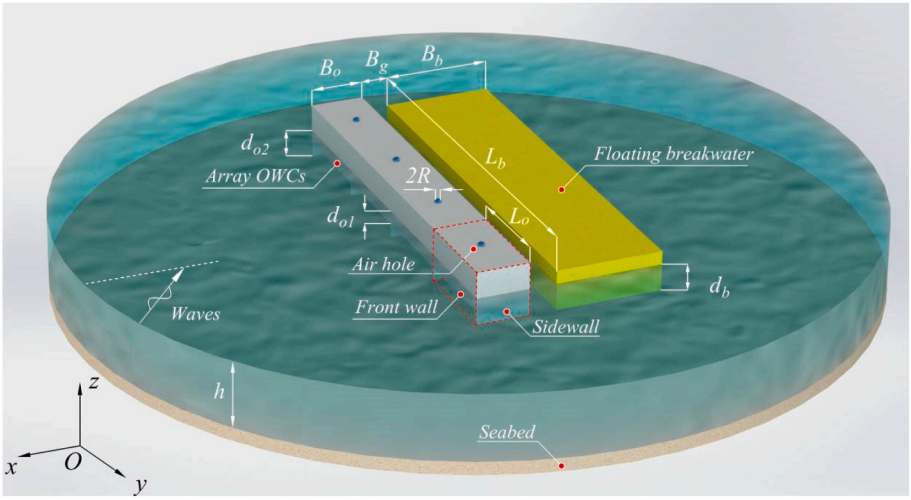

Fig. 1. Schematic of an array of box-type OWCs parallelly installed at the facing-wave side of a very long flexible floating breakwater.

hybrid system consists of WECs and an OWT, indicating that the peak output power can be significantly improved from 16.7 MW to 117 MW. Secondly, the overall construction cost will be reduced by sharing mooring lines, supporting devices, grid connections and maintenance equipment. As pointed out by Falcão et al. [7], the Levelized Cost of Energy (LCOE) of wave energy can be substantially reduced by integrating wave and offshore equipment. Thirdly, WECs can replace fossil fuels to meet the daily energy needs of offshore platform automation, due to low costs and high environmental friendliness. For example, WECs can satisfy the daily power consumption (4.78 kW h) of a typical single column-dual row offshore cage [8]. Fourthly, an efficient layout of WECs along the periphery of offshore structures can reduce the transmitted wave height and provide a mild wave environment downstream, which reduces the motion response of floating bodies. Meanwhile, since reflected waves from offshore structures can cause constructive effects, the power harvesting capacity of WECs can be potentially enhanced. Therefore, integrating WECs into offshore structures can generate significant synergies.

To fully exploit the synergistic effects of the integrated system in wave attenuation, combining different type WECs with floating breakwaters is an effective way. There are usually two ways to integrate a OB-type WEC with a breakwater: 1) Mechanically connecting an OB type WEC with a breakwater. 2) treat a breakwater as the floater of a WEC and extract energy from the motion of the breakwater. Considering the simplicity of design and the development potential of Pile-constrained Floating Breakwaters (PFBs), Ning et al. [9] proposed to integrate a hydraulic PTO system into a PRFB. Garnaud et al. [10] demonstrated that several small buoys have better energy conversion performance than a single buoy with the same total volume. Subsequently, Ning et al. [11] optimized their previous design of a dual-buoy integrated system, experimental results indicated that the integrated system can broaden the frequency bandwidth within which the energy conversion efficiency is higher than 0.3, compared to a sigle buoy. Favaretto et al. [12] found that there is a phenomenon of superposition of incident and reflected waves on the facing-wave side of a breakwater, amplifying the energy conversion efficiency of WECs. On this basis, Zhao et al. [13] designed a hybrid system consisting of an OB-type WEC deployed on the weather side of a breakwater and pointed out through experiments that the efficiency of the WEC arranged on the breakwater heading-to-wave measurement was significantly improved compared to isolated cases. As an extension, Ning et al. [14] investigated the wave extraction capability of an array of WECs arranged on the weather side of a fixed breakwater. This study discovered the presence of zero efficiencies at certain wave frequencies. In order to explain this experimental finding,

Ouyang et al. [15] followed up with a numerical simulation and concluded that the destructive effect of the Bragg resonance triggered by the integrated system leads to the sudden reduction in energy conversion efficiency. Madhi et al. [16] proposed a multi-functional structure called "The Berkeley Wedge" (TBW), which contains a floating wedge-shaped breakwater with different front and rear drafts. Corresponding studies showed that the design of the asymmetric wedge resulted in very small radiated waves on the lee side compared to conventional devices with symmetrical drafts, which facilitated an increase in energy conversion efficiency [17]. Subsequently, to further explore the potential of the TBW, Madhi and Yeung [18] analyzed the survivability of the TBW under extreme conditions. Tay [19] proposed a novel array of raft-type WECs integrated with a long floating breakwater and implemented a frequency-domain numerical study. The results show that the hydroelastic response of the floating breakwater affects the wave energy extraction of WECs. Cheng et al. [20] examined numerically the wave energy extraction of modular OB-type floating breakwaters deployed at the facing-wave side of a very large floating structure, demonstrating that WECs can provide the synergy between energy extraction and hydroelastic reduction.

As a simple and robust WEC, OWC-type WECs also have attracted numerous scholars to study the feasibility of integrating with floating breakwaters. Koo [21] designed a floating box breakwater with an air chamber in the middle to form an OWC device and investigated its wave attenuation performance. Thanks to the excellent performance of the aerodynamic damping for dissipating wave energy, this structure has a smaller transmitted coefficient compared with conventional box-type breakwaters. Zhao et al. [22] experimentally compared the hydrodynamics of OWC devices with different chamber numbers, and found that multi-chamber OWC possesses higher energy conversion performance. He et al. [23] discerned experimentally the performance of a floating breakwater with OWC chambers on both front and back sides, and concluded that an asymmetrical configuration of front and back chambers can cause larger pneumatic pressure. Furthermore, He and Huang [24] proposed a plie-based breakwater-OWC integrated system and concluded that the new concept not only has good wave absorption performance, but also generates an air-pressure difference in the chamber suitable for converting wave energy into electricity. Sundar et al. [25] also developed a novel floating breakwater incorporating a U-OWC device. The superiority of the U-OWC over other OWC devices has been confirmed by many theoretical and experimental studies [26]. Unlike conventional OWCs, the U-OWC with a vertical duct prevents the propagation of incident waves into the inner chamber and uses the vertical motion of the water at the duct opening to create a new form of excitation, which results in a longer eigenperiod of the U-OWC and a higher pressure inside the air chamber [27]. In addition, the U-OWC can improve the safety of the device by avoiding sand entering the chamber which may reduce air inhalation at the bottom opening [28]. The results show that the air-storage chamber is embedded inside of a floating breakwater without changing the geometry shape of the base structure, and an air turbine is necessary to be installed at the roof of each chamber, meaning that the structural reliability can be maintained and the construction cost is low. There are already some practical engineering applications of integrated OWC-type WECs and breakwaters in the world. For example; the Pico wave energy plant, rated at 31.7 kW, in Portugal [29], the Ocean Swell Powered Renewable Energy (OSPREY) OWC plant, rated at 2 MW, in Japan [30], and the Land Installed Marine Powered Energy Transformer (LIMPET) project, rated 113 kW, in Scotland [31].

Moreover, advanced theoretical, numerical, and experimental methods have been widely used for simulating the hydrodynamic performance of a hybrid system incorporating OWC devices and floating breakwaters. Based nonlinear potential flow theory, Martins-Rivas and Mei [32] conducted an analytical study on the hydrodynamic performance of an OWC device installed on a breakwater by matching eigenfunction. Tsai et al. [33] presented a three-dimensional (3-D) Computational Fluid Dynamics model (CFD) to investigate the influence of front wall submergence, orifice size and porosity of perforated front wall on a modified breakwater-integrated OWC device including a perforated front wall. Later, by using a 3D time domain model, Zhou et al. [34] analyzed the coupled hydrodynamic response of an OWCintegrated into an OWT and compared OWC response and corresponding air pressure with experimental data. Considering the synergistic effect of multiple OWCs and a breakwater, Zheng et al. [35] developed a 3-D analytical model to evaluate the impact of an array OWC integrated into a breakwater in terms of system efficiency. Elhanafi et al. [36] pointed out that the draft of the front lip of an OWC device can significantly alter the wave energy capture efficiency by investigating the water surface motion inside the chamber of a breakwater-OWC integrated device using the Volume of Fluid (VOF) method. Through viscous-flow CFD simulations, Majani et al. [37] demonstrated that the energy extraction of the expiratory mode in the chamber of an OWC device chamber was lower than that of the inhalation mode. Deng et al. [38] explored the effect of a horizontal bottom plate with a certain thickness on the wave energy capture efficiency of a breakwater-OWC integrated system using a CFD solver OpenFOAM.It was concluded that by selecting a proper horizontal bottom plate, the efficiency of the OWC can be increased. Based on the Reynolds-Averaged Navier-Stokes (RANS) equation, Elhanafi et al. [39] established a 3-D CFD model to compare the energy extraction efficiency of a single-chamber OWC and a dual-chamber OWC devices. Results indicated that the dual-chamber OWC has a higher wave energy conversion efficiency when subject to medium and long wavelengths. Kuriqi et al. [40] elaborated a relationship between energy production and ecosystem conservation. Furthermore, Kuriqi and Jurasz [41] reviewed the current status of renewable energy production and emphasized the objective of maximizing water power profitability while ensuring "good" ecological status. Cheng et al. [42] adopted fully nonlinear wave theory to investigate the effect of a gap between OWC and floating breakwater on wave energy conversion. It was found that wave resonance in the gap would lead to a sudden reduction of wave energy harvesting efficiency. Following this study, Cheng et al. [43] compared the power extraction and wave attenuation performance of an OWC-type dual-pontoon breakwater and an OB-type single-pontoon breakwater. The study concluded that the hydrodynamic performance of the OWC-type breakwater is superior to that of the OB-type breakwater with the same pontoon width and mass. Howe et al. [44] presented an experimental investigation on a floating breakwater with an array of OWC chambers. It was revealed that wave energy conversion from OWCs can be improved within a range of wave frequencies due to the constructive array effects. Furthermore, Howe et al. [45] experimentally tested the motion characteristics of the floating breakwater. The results identified that the wave interaction of chambers influences the breakwater motions.

Existing studies gave enlightening contributions in the configuration design and performance analysis of the WEC-floating breakwater integrated system, but focused mainly on rigid floating systems. In practical engineering, in order to provide sufficient shielding area and achieve a favourable wave attenuating efficiency, a floating breakwater system is usually assembled by connecting multiple individual modules, leading to very long floating systems. The high aspect ratio in the longitudinal and transvers dimensions suggests that the elastic deflections of such floating bodies should be considered. Additionally, the inhomogeneous wave characteristics distributed along the very long structure can result in non-negligible hydroelastic response, especially for oblique incident wave conditions. Therefore, in this work, a design of integrating multiple rectangular box-type OWCs at the facing-wave side of a very long-flexible floating breakwater is proposed. Where an in-line array of OWC devices is deployed along the length of the floating breakwater. The novelty and contributions of this work are twofold: firstly to develop a two-way fluid and structure coupled hydroelastic model to investigate the effect of breakwater structural deformation, and secondly to assess both wave energy conversion and wave attenuation performance of the

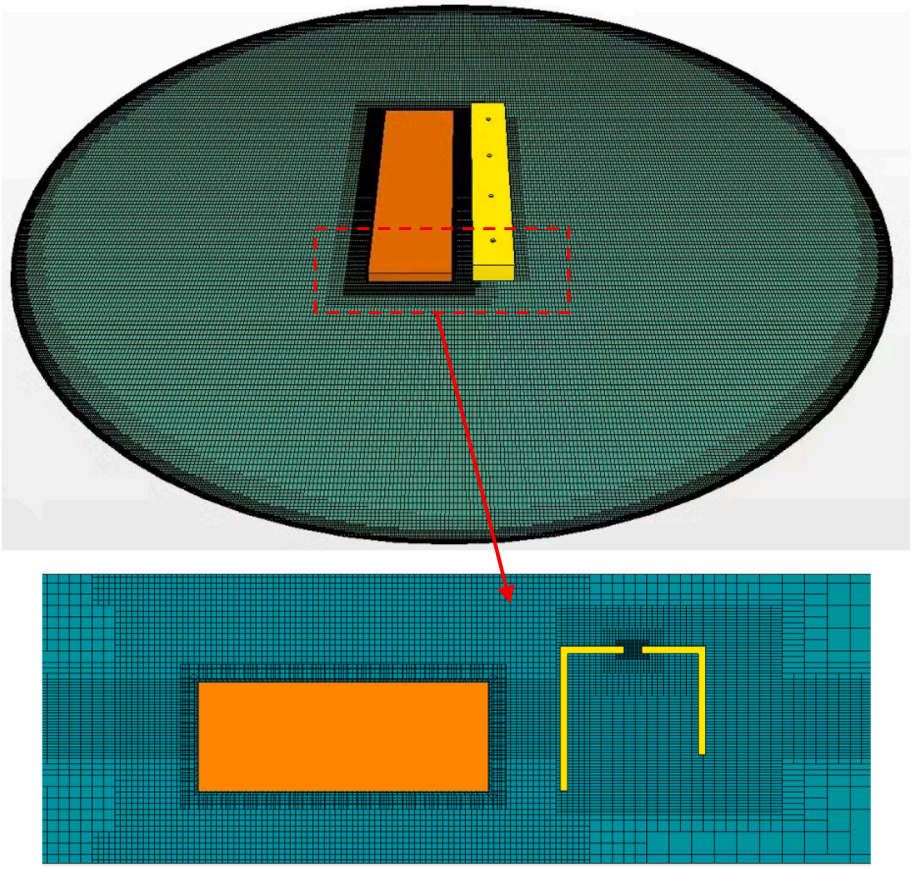

Fig. 2. Numerical computational domain.

integrated system.

. The developed methodology consists of both CFD and FEM, where the CFD is used to solve the fluid problem while the FEM is used to realise the structure coupling.Hydrodynamic comparisons of the integrated system with different designed parameters, i.e. OWC number, OWC-breakwater gap distance, OWC draft, breakwater bending stiffness and incident wave angle are also examined in the current work.

The rest of the study is structured as follows. Section 2 describes the development of a CFD-FEM hybrid model which includes the principles of compressed air-water-solid interaction, rigid-flexible coupling motions and multi-body interferences. In Section 3, the developed numerical model is validated. In Section 4, the parametric sensitivity analysis is presented, which mainly focuses on the optimal configuration of OWCs within the integrated system and the contribution of the hydroelastic response of the flexible breakwater to wave resonance in the OWC chamber and OWC-breakwater gap. Finally, the conclusions are drawn in Section 5.

2. Mathematical model

In the numerical simulation, four box-type OWCs are parallelly deployed along the facing-wave side of a very long flexible floating breakwater with a bending stiffness EI (where E denotes the elastic modulus and I is the cross-section rotational inertia), as shown in Fig. 2. The floating breakwater is a single pontoon-type hexahedron with a length of L_b, a width of B_b and a draft of d_b. Deflection of the breakwater is restricted to vertical direction only in this study. The mooring system is ignored in the present work as a mooring system for such kind of devices mainly prevents the device from drifting away and has little effect on the device's motion response. In order to examine the hydroelastic effect of the floating breakwater on the wave energy extraction of OWCs, OWCs are assumed to be stationary. All OWCs have the same geometrical sizes, i.e. identical chamber length L_o, chamber width B_o, draft d_{o1} of the front wall, and draft d_{o2} for the other walls, and are numbered in ascending order along the global positive y-direction (see Fig. 1 for the coordinate system). The total length of all the chambers is set to be same as the breakwater length, i.e. $L_b = N \times L_o$. The gap distance between the OWC and the breakwater is denoted by B_g. The scattering waves generated by the floating breakwater can induce multi-mode wave resonance in the OWC chambers and is the research motivation of this work. The overall WEC-floating breakwater integrated system is established in a cylindrical computational domain with a water depth h. A fully nonlinear CFD-FEM hybrid model is developed to accurately solve the above hydrodynamic problems, which is a two-way coupling simulation between fluid and structure. Compared with the traditional one-way coupling simulation [46and47], the two-way coupling simulation does not only consider the effects of water motion on the structural deformation, but also captures the hydroelastic scattering waves around the structure which can affect significantly the wave energy extraction of OWCs. Other advantages of the proposed advanced numerical method include the consideration of the fluid viscosity in the CFD model and the solution of the precise vibrational modes in the FEM model, avoiding unexpected inaccuracy and divergency during directly simulating the hydroelastic wave resonance in the WEC-breakwater gap. This section summarizes the numerical model briefly and detailed solution procedures are referred to Ref. [48].

2.1. Fluid simulation

According to the physical characteristics of the flow field, the fluid motion is assumed to be governed by RANS equations [49], which satisfies the continuity, momentum, space-conservation and transport conditions of scalar quantities. A suitable turbulence model which provides the closed relationship for the RANS equations should be employed to simulate strictly the energy dissipation. In this work, the realizable *k*-epsilon two-layer model is selected to obtain the turbulent kinetic energy *k* according to the values of the strain tensor **P**

$$K_t = 2\mu_t \mathbf{P} - \frac{2}{3}(\mu \nabla \times \mathbf{v} + \rho_w k)\mathbf{I} \tag{1}$$

where $\mathbf{K_t}$ is the eddy viscosity term, μ is the viscosity, **v** is the flow velocity vector, **I** is the identity matrix and ρ_w is the water density. The two-layer model is an alternative approach to solving low Reynold numbers, which can add the *k*-epsilon model into the viscosity layer. In this model, the layer is divided into two layers which are defined as the near-wall layer and the away-wall layer according to the wall distance $d+$

$$d+ = \frac{d}{v}\sqrt{\frac{\tau_w}{\rho_w}} \tag{2}$$

where d is the wall distance from the first prism layer, v is the kinematic viscosity and τ_w is wall shear stress. Thus, in the near-wall layer, the turbulent variables i.e. dissipation rate ε and viscosity μ_t are expressed as functions of the wall distance $d+$, which are transferred smoothly to the values calculated from the transport equation in the away-wall layer. On the other hand, the turbulent kinetic energy equation is solved within the total computational domain.

The computational domain is discretized using the Finite Volume Method (FVM) which solves the integral forms of governing equations in a finite number of Control Volumes (CVs). The corresponding physical variables are satisfied in the cell centres of CVs. Additionally, the water surface is captured by calculating the volume fraction σ of the water or air into each CV, i.e. $\sigma = 0$ means that a CV is filled with only air and $\sigma = 1$ is full of water. When σ falls into the range of 0–1, there exists a water-air interface which is simulated using the High-Resolution Interface Capturing (HRIC) discretization approach. A first-order upwind difference scheme is adopted to solve the transport equation of air or water as follows

$$\frac{\partial}{\partial t}\int_V \sigma_i dV + \oint_A \sigma_i v \times dA = \int_V S_i - \frac{\sigma_i}{\rho_i}\frac{d\rho_i}{dt}dV - \int_V \frac{\sigma_i}{\rho_i}\nabla\left(\sigma_i \rho_i \mathbf{v}_{d,i}\right)\frac{d\rho_i}{dt}dV \tag{3}$$

where $i = w$ denotes water and $i = a$ denotes air. V and A denote the volume and surface integrals, respectively. $\mathbf{v}_d$ is the diffusive velocity, S_i is the user-specified source term.

The boundary condition of the lateral side is set as velocity inlet which is prescribed by the fifth-order Stokes wave combined with a wave forcing method to eliminate the reflected waves. The top of the computational domain is defined as the pressure outlet which is a Neumann condition where the airflow is fully developed and thus no fluctuations and reflections occur. The bottom boundary is a no-slip wall condition where the normal velocity is zero and thus there is only tangential velocity of the flow along the wall surface. Cartesian hexahedral meshes with trimmed cells are selected to discretize the whole computational domain. At the water surface, 20 and 80 meshes per wave height and wavelength are equally distributed along the vertical and horizontal directions, respectively. An overset mesh scheme is chosen to resolve the wave-induced motion of the proposed hybrid system. This mesh scheme consists of two sets of meshes: a spatially fixed background mesh contains only fluid, and an overset mesh which can move freely with the hybrid system (as if the system is a rigid body) The overset mesh is deployed inside the background mesh. During simulation, fluid information is exchanged between the background mesh and the overset mesh through interested meshes. Inside the overset mesh, a mesh morphing scheme is adopted to account for the structure deformation of the breakwater, i.e. individual cells inside the overset mesh will deform in shape and volume when the breakwater exhibits deformation.

2.2. Structural simulation

The structural motion equation of hybrid system is established according to the Hamiltonian principle

$$\delta \int_{t_0}^{t} (U - H + W)dt = 0 \tag{4}$$

where U, H and W denote the elastic strain energy, the kinetic energy and the potential energy, respectively. The FEM is used to discretize the wetted surface of the floating breakwater into a series of rectangular membrane elements which are subjected to fluid loads and are connected to a hull beam by imposing kinematic coupling constraints. The hull beam is defined as a regular rectangular section whose dimensions are determined by the vertical bending stiffness of the floating breakwater, and hence its nodal displacement w is expressed by superposition of the natural modes

$$w = \sum_{i=1}^{m} \zeta_i(t)\{D_i\} \tag{5}$$

where ζ_i and D_i denote the i-th modal amplitude and natural mode vector; m is the first mode number. The first six modes i.e. $\{D_i\}(i = 1,2,3,4,5,6)$ represent the six-degree-of-freedom rigid body motions including surge, sway, heave, pitch, roll and yaw, and the rest correspond to flexible modes of the floating breakwater. In this work, only the heave responses including rigid motion and elastic deformation of the floating breakwater are considered, and other horizontal motions are assumed to be restrained by mooring systems. The global motion equation can then be obtained from Eq. (4)

$$[M]\{\ddot{w}\} + [C]\{\dot{w}\} + [K]\{w\} = \{F\} \tag{6}$$

where $\{w\}$ is the displacement vector, $[F]$ nodal load vector obtained by CFD solutions, $[K]$ is the global bending stiffness matrix, $[M]$ is the global mass matrix and [C] is the global damping matrix. A Rayleigh damping model [50] is applied to approximate the structural damping matrix

$$[C] = \gamma[K] + \mu[M] \tag{7}$$

where γ and μ are the damping coefficients which are proportional to the stiffness and mass, respectively. These are associated with the critical damping ξ

$$\xi = \frac{\gamma\lambda}{2} + \frac{\mu}{2\lambda} \tag{8}$$

where λ is the eigenvalue corresponding to the modal shape.

Substituting the modal expansion Eq. (5) of the vertical displacement into Eq. (6), the motion equation can be assembled as follows

$$[M][D]\{\ddot{\zeta}\} + [C][D]\{\dot{\zeta}\} + [K][D]\{\zeta\} = \{F\} \tag{9}$$

where $[D]$ is the matrix corresponding to natural modes, ζ is the time-dependent modal amplitude vector. The natural modes are accurately captured by solving straightway the following eigenvector equation of a vibrating beam in dry air, rather than being explicitly set as orthogonal beam functions or Legendre polynomials.

$$[K][D] = [\lambda][M][D] \tag{10}$$

where [λ] is the eigenvalue matrix.

Then, Eq. (9) is pre-multiplied by the transposition matrix $[D]^T$, and can be generalized as follows

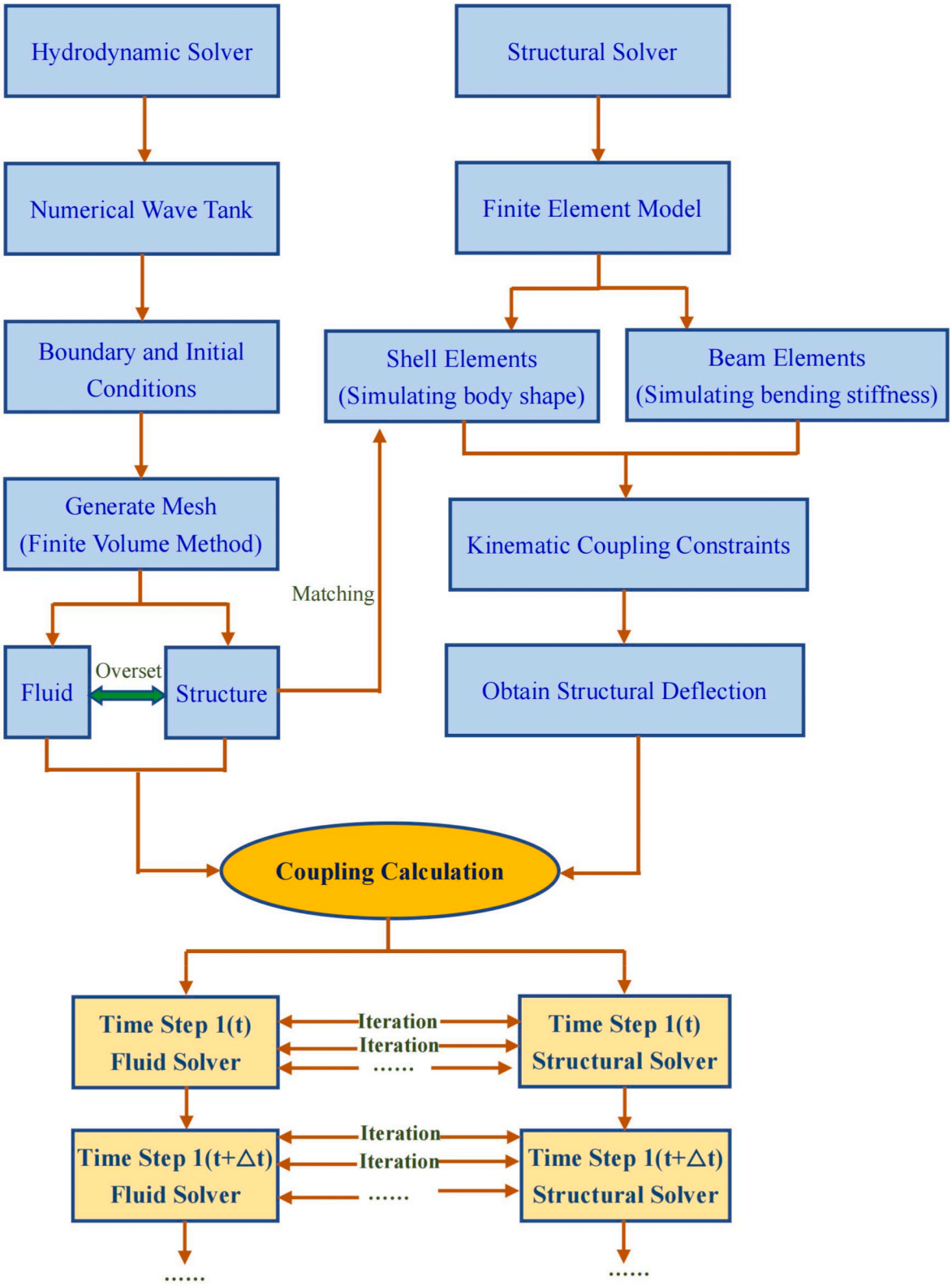

Fig. 3. CFD-FEM coupling process.

$$[D]^{\mathrm{T}}[M][D]\{\ddot{\zeta}\}+[D]^{\mathrm{T}}[C][D]\{\dot{\zeta}\}+[D]^{\mathrm{T}}[K][D]\{\zeta\}=[D]^{\mathrm{T}}\{F\} \tag{11}$$

After Eq. (11) is solved by using a time-marching approach i.e. the fourth-order Runge-Kutta scheme, the modal amplitude is substituted back into Eq. (5) to respond to the flow field around the integrated system.

2.3. CFD-FEM coupling procedure

In general, the interaction of the waves and the integrated system includes two parts: rigid body interaction and elastic body interaction, and hence the fluid and structural solvers should be operated in a coupled approach. A one-way coupling approach can provide

reasonable solutions for the rigid motions with a less computational resource, but does not capture the scattering waves generated by the flexible deformations. Additionally, the one-way coupling is only applicable if the deformation of the structure has a very small effect on the fluid. The additional mass induced by the fluid motion is evaluated based on empirical formulas which are uniformly used on the submerged surfaces and can not consider fluid interaction with structural deflections. In this work, the deformation of the floating breakwater is not negligible and apparently affects the wave propagation along the WEC-floating breakwater integrated system. Therefore, a two-way coupling approach is adopted, in which the structural deflection is fed back into the fluid solver to update the mesh near the body. The whole motion equations for both the fluid and the structure are simultaneously solved by iterating back and forth in a cylindrical computational domain, as shown in Fig. 2. The two-way coupling can be further classified into explicit and implicit coupling schemes which are appropriate for a steady-state solution where the motion velocities of the bodies are approach very small or even zero and a transient-state solution where the mutual dependence between fluid and bodies is high at each time step, respectively. In this work, the implicit coupling scheme is adopted to exchange information including pressure, velocities and deflections between fluid and structure solvers more than once at each time step, the simulation will only march to the next time step when residual of the previous time step is less than 0.001.

The fluid motion is simulated in the CFD software Star-CCM+, which is used to conduct co-simulations (coupled) of wave-structure interactions with a finite element solver, i.e. Abaqus, as shown in Fig. 3. In the structural model, the wetted surface of the floating breakwater is discretized into 2834 4-node quadrilateral membrane elements, and the bending beam is simulated using 60 Timoshenko beam elements. The number of data exchanges between fluid and structure is defined as 8 at each time step so that the co-simulation displacements converge in a coupled iteration, which is critical for the accuracy and computational cost of the fluid-structure interaction. The fluid pressures are transferred from the CFD solver to the FEM solver which calculates the structural displacement to feedback to the CFD solver. The geometry and coordinates of the floating body are updated simultaneously in both software. The grid flux Under Relaxation Factor (URF) related to the motion of fluid meshes according to the structural deflections is reduced from the default value of 1.0 to 0.8 to provide numerical stability. Grid adaptation in the CFD model is implemented using mesh morphing to follow the structural deflection based on the cluster or scatter of mesh nodes obtained by the structure solver. The interpolation techniques are applied to map the data from one solver to the other, which are decided based on whether the source data is face-centric or node-centric The overset grid interfaces move in response to the interpolation field calculated by the morphing motion.

2.4. Energy conversion

The hydroelastic response of the floating breakwater generates multi-mode radiated waves which affect the water oscillation and the airflow in OWC chambers. There is a circular orifice installed at the top of each chamber to model the damping effect of a PTO system. The air pressure p_{ai} existing inside i-th OWC chamber is expressed as

$$p_{ai} = \frac{1}{2}\rho_a C_d \left| U_{ai}(t) \right| U_{ai}(t) \tag{12}$$

where $U_{ai}(t)$ is the airflow velocity through the orifice. In Eq. (12), the right-hand term is the pressure drop due to the PTO, which results in the loss of air pressure. Quadratic pneumatic damping coefficient C_d is determined by

$$C_d = \left(\frac{1}{\alpha C_c} - 1 \right)^2 \tag{13}$$

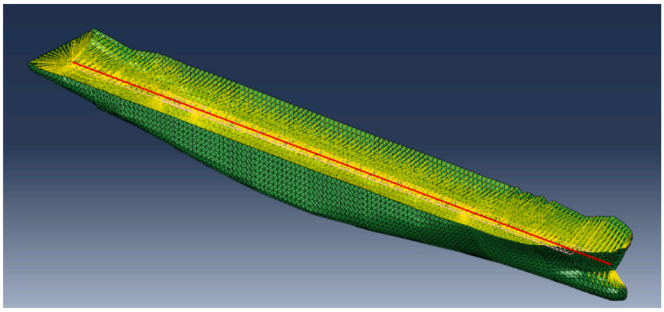

Fig. 4. FEM model of a 6750-TEU containership.

where α is the opening ratio of the orifice, which is assumed to be identical for all chambers. C_c is the shrinkage coefficient and can be approximated by taking the average value of $C_c = 0.61$ for a thin-walled circular orifice. Thus the period-average power extraction by the i-th OWC device can be expressed as:

$$E_{pi} = \frac{A_o}{T} \int_{t_0}^{t_0+T} \sqrt{\frac{2|P_{ai}(t)|^3}{\rho_a C_d}} dt \tag{14}$$

where T is the incident wave period, A_o is the horizontal water area in each chamber. The total extracted power E_p^{total} by all chambers can be obtained

$$E_p^{total} = \sum_{i=1}^{N} E_{pi} \tag{15}$$

The energy conversion efficiency R by the array OWCs can be calculated as follows

$$R = \frac{E_p^{total}}{E_w^{total}} \tag{16}$$

where E_w^{total} denotes the incident wave energy along the propagating direction perpendicular to the breakwater length and is written for regular incident waves as:

$$E_w^{total} = \frac{1}{16} N \cdot L_o \cdot \cos\theta \cdot \rho_w \cdot g \cdot H_I^2 \cdot \frac{\omega}{k} \cdot \left(1 + \frac{2kh}{\sinh 2\,kh} \right) \tag{17}$$

where g is the gravity acceleration, ω is the wave frequency, H_I is the incident wave height, θ is the incident wave angle with respect to the positive x-axis direction, $k = 2\pi/\lambda$ is wave number, λ is the wavelength.

The wave attenuation capacity of the integrated system is quantified by the transmission coefficient K_t downstream the breakwater

$$K_t = \frac{H_t}{H_I} \tag{18}$$

where H_t is the transmitted wave height downstream from the breakwater.

In order to describe the hydroelastic response distribution along the floating breakwater, the nodal displacement Eq. (5) can be rewritten in terms of the Response Amplitude Operator (RAO)

$$w_0 = \frac{2w_{\max}}{H_I} \tag{19}$$

where $w_{\max}$ is the maximum value of the hydroelastic response.

3. Modal validation

3.1. Hydroelastic response comparison

In order to examine the accuracy of the CFD-FEM hybrid method for

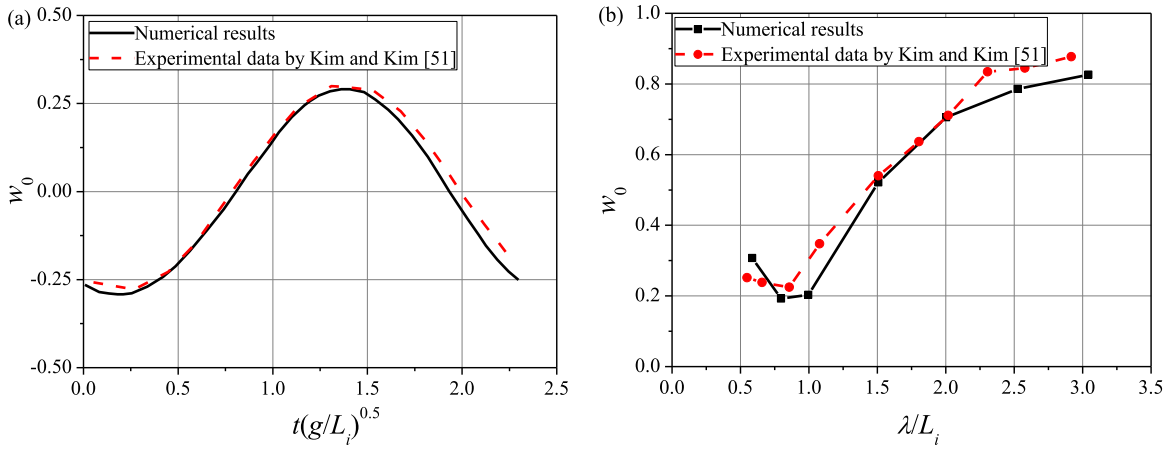

Fig. 5. Comparison of numerical and experimental results (a) hydroelastic time series at $T\,(g/L_i)^{0.5} = 1.49$ and (b) hydroelastic RAO variation against wavelength.

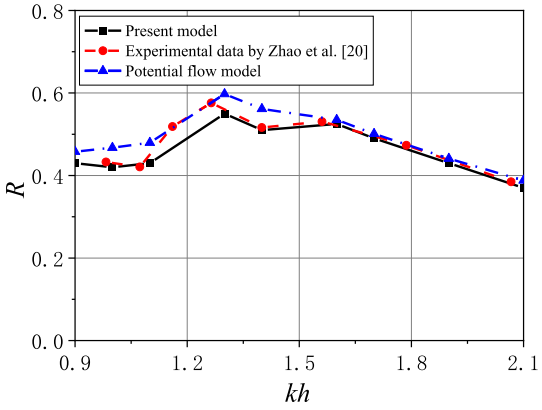

Fig. 6. Numerical and experimental comparison of wave energy conversion efficiency.

solving the hydroelastic response, a 6750-TEU containership with a scale ratio of 1:70 is considered in this section, and its hydrodynamic experiments have been conducted by Kim and Kim [51]. The experimental model has an overall length of $L_s = 4.298$ m, an inter-vertical length of $L_i = 4.094$ m, a ship width of $B_s = 0.571$ m, and a ship height of $d_s = 0.346$ m, inside which a uniform steel beam with bending stiffness $EI = 5.95 \times 10^4$ Nm^2 is fixed to simulate the hull beam of this containership. The present numerical model is shown in Fig. 4 using a total number of 12,618 elements. Fig. 5(a) shows comparisons of the time series of the hydroelastic RAO between the present solutions and the experimental data. The input wave parameters are $H_I = 0.088$ m and $T = 0.95$ s ($\lambda = 4.381$ m). It can be seen that the numerical solutions match well with the measured data in both values and trends. Furthermore, comparisons of the hydroelastic RAO against dimensionless wavelength λ/L_i are shown in Fig. 5(b). The slight differences in certain periods can be attributed to the simplifications of the physical model i.e. the mass distribution of the hull and the uniform steel beam model. Overall, the good agreement suggests that the present hybrid numerical model can efficiently assess the trend of the hydroelastic RAO of flexible floating bodies.

3.2. Energy conversion comparison

Wave energy conversion of the OWC device simulated by the present CFD model is validated based on experiments of a triple-chamber OWC manufactured by Zhao et al. [20]. Fig. 6 shows comparisons of the energy conversion efficiency R against dimensionless wave number *kh*. The input parameters are: chamber draft $d_{o1} = d_{o2} = 0.2$ m, chamber width $B_o = 0.64$ m, opening ratio $\alpha = 1.0\%$, wave height $H_I = 0.05$ m and water depth $h = 0.6$ m. In order to compare the performance of different models, results provided by a potential model [40] are also presented in this figure. From the figure, it can be found that the present numerical model captures accurately the efficiency peaks and their occurring

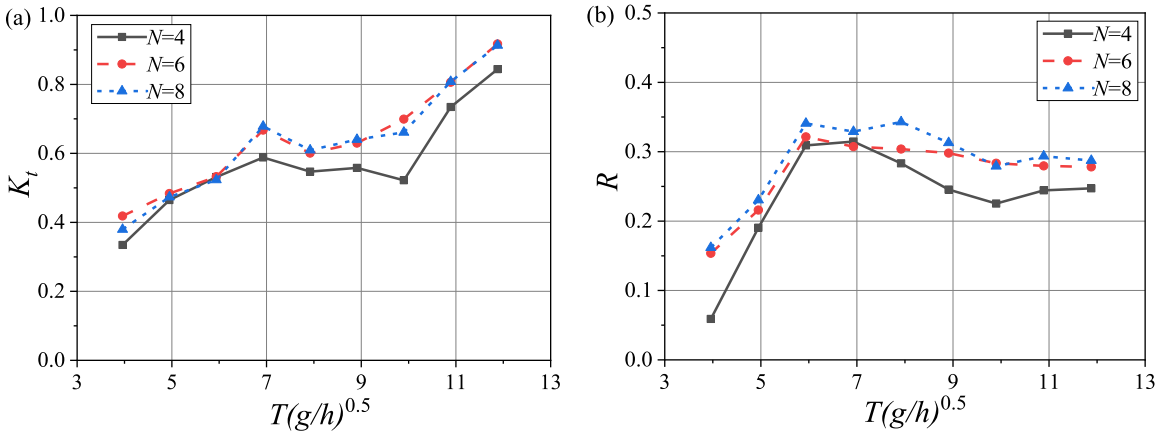

Fig. 7. (a) Transmission coefficient and (b) overall energy conversion efficiency against wave period and chamber number.

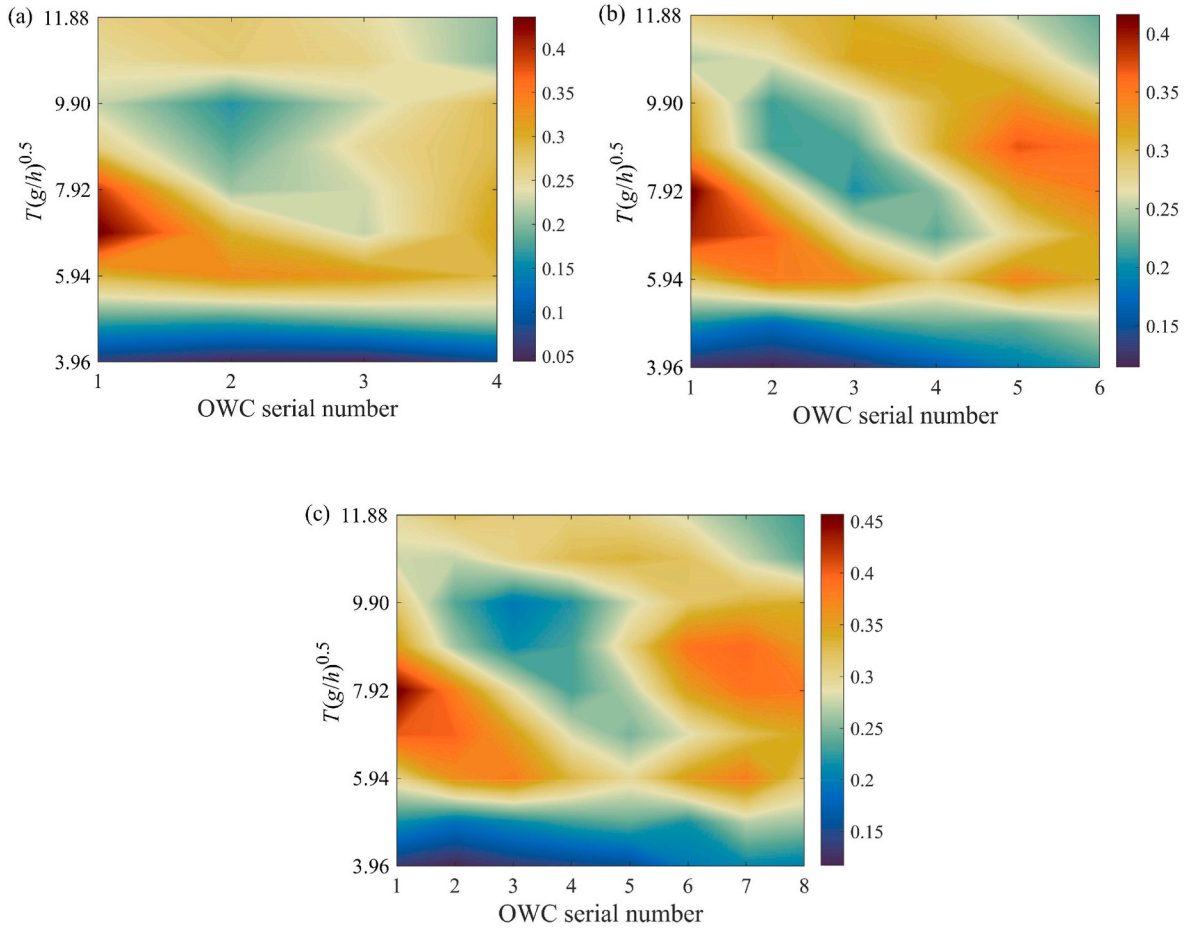

Fig. 8. Efficiency contour of different chambers i.e. (a) four chambers, (b) six chambers and (c) eight chambers.

locations i.e. resonant periods. In addition, the present model is in better agreement with the experimental data than the potential flow model. The latter over-predicts the power extraction, especially in long-period waves. This may be because the viscous effect of fluid is neglected in the potential flow model. In particular, an accurate energy conversion efficiency is evaluated by the present model in which the water motion in the OWC chamber is simulated by using the FVM, and the air compressibility induced by the Well turbine is taken into consideration.

4. Numerical results

Based on the presented CFD-FEM coupling method, the hydrodynamic performance of a very long flexible floating breakwater integrated with an array OWCs is investigated, including the transmission coefficient, the energy conversion efficiency, the hydroelastic response and the wave field around the integrated system. Unless it is specified, the geometric parameters of the floating breakwater are given as $L_b \times B_b \times d_b = 60$ m $\times$ 16 m $\times$ 4 m and $EI = 1.53 \times 10^{10}$ Nm^2. The number of OWCs installed at the facing-wave side of the floating breakwater $N = 4$, and has identical dimensions as $d_{o1} = 2$ m, $d_{o2} = 4$ m, $L_o = 15$ m, $B_o = 8$ m and $\alpha = 0.625\%$. Wave conditions are: $H_I = 3.5$ m, $h = 10$ m and $T = 4$ s–12 s ($\lambda = 28.5$ m–117.9 m). After the convergence tests with mesh size and time step are completed, minimal element length $l_e = \lambda/20$ and time step d$t = T/50$ are selected in the following simulation. The configuration of the OWCs as a function of the OWC number, and the spacing distance between the OWC-breakwater and the sidewall draft of the OWC is elaborated. The resonant characteristics of the water in both the OWC chamber and the OWC-breakwater gap are examined. Furthermore, the influences of the bending stiffness of the breakwater and the incident wave direction are studied to illustrate the relationship between the wave energy conversion and the hydroelastic response.

4.1. Effect of the number of OWC chambers

This subsection considers the different number of OWC chambers i.e. $N = 4$, 6 and 8 which corresponds with chamber length $L_o/h = 1.5$, 1 and 0.75, respectively. Fig. 7(a) and (b) plots the variation of the transmission coefficient and the overall energy conversion efficiency with wave period for different chamber numbers. It is evident from Fig. 7(a) that within the simulated wave period range, the transmission coefficients are almost identical for $N = 6$ and 8, and are generally larger than those for $N = 4$, especially for long-period waves ($T(g/h) > 6$). This is because the characterized dimension of the OWC interacting with waves is determined by both the OWC length and the OWC width in the cases of obliquely propagating waves (i.e. $\theta = 45°$). Compared with $N = 6$ and 8, $N = 4$ has the largest chamber plane area in which the water column can easily enter to trigger piston-type and sloshing-type resonances, leading to more energy dissipation. This is to say, the resonance modes in chambers are strongly related to the relative dimension of the chamber to the wavelength. Additionally, this allows for the conjunction of the crest and trough portions inside the chamber. Thus, the rising and falling liquid levels cancel with each other, and the compressibility of the air is reduced, demonstrating that the multiple OWCs have better overall energy conversion performance as shown in Fig. 7(b). Compared Fig. 7(a) and (b), it can be concluded that the configuration of multiple OWCs integrated with the floating breakwater could be preferred to extract full wave energy from constructive array effects, but does not contribute much to the attenuation capacity of the breakwater.

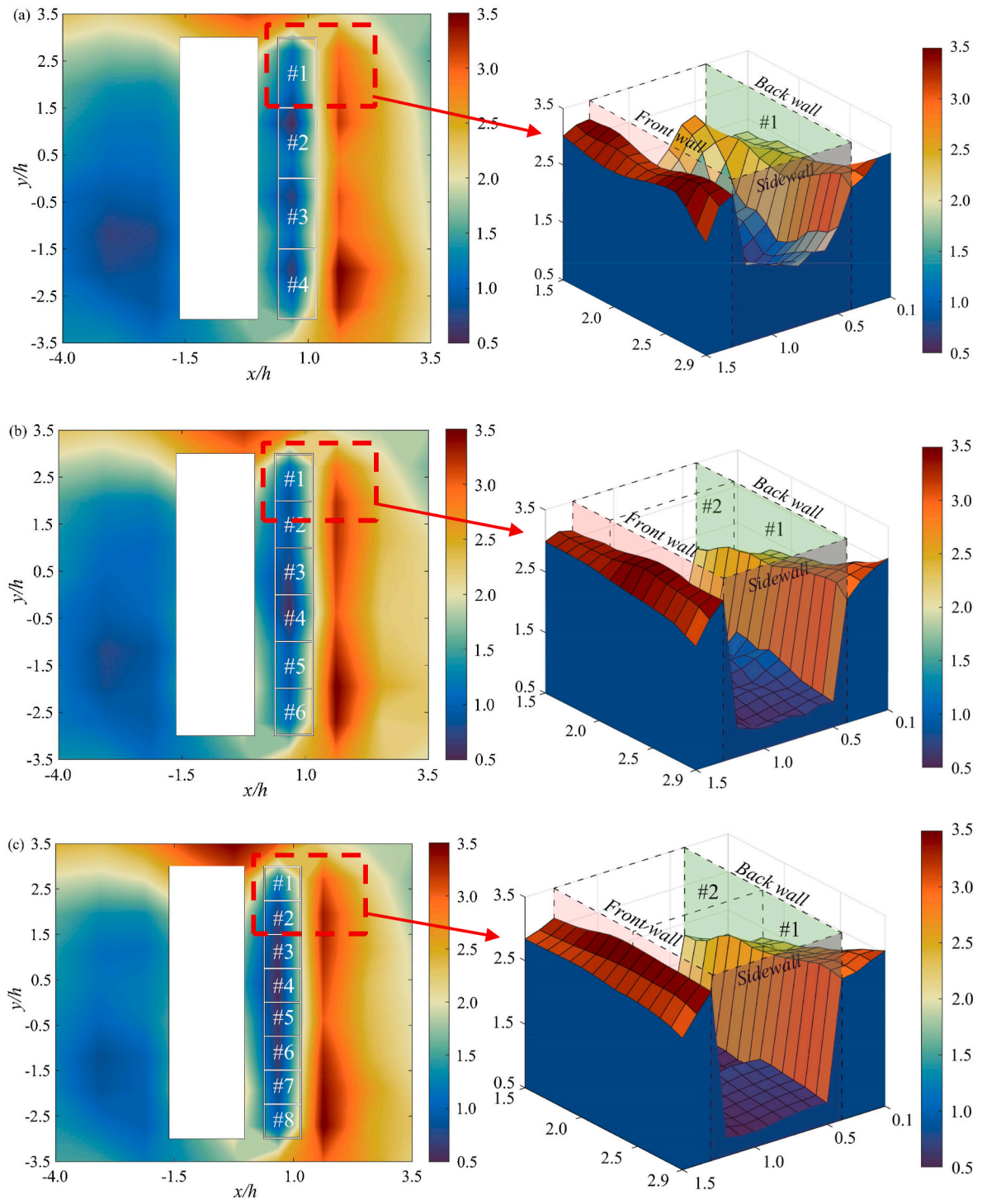

Fig. 9. Wave amplitude distribution around the breakwater-OWC integrated system i.e. (a) four chambers, (b) six chambers and (c) eight chambers.

In order to further illustrate the energy conversion of each chamber, the efficiency contour as a function of wave period and number of OWCs is shown in Fig. 8(a)–(c) for different configurations. From the perspective of maximum energy conversion, it is remarkable that the chamber closer to the incident wave direction extracts more wave energy for $N = 4$ in the moderate wave periods ($5.9 < T(g/h)^{0.5} < 8$) range, as shown in Fig. 8(a). This is because the wave energy is gradually absorbed by OWCs along the wave propagating direction, and the shielding effect also hinders the OWC performance at the middle location. As the number of OWCs increases, the discrepancy in efficiency between chambers becomes more pronounced, especially for $N = 8$. As shown in Fig. 8(c), the chambers at both ends have better energy extraction in the range of wave periods ($5.9 < T(g/h)^{0.5} < 10$), while those at the middle location are more effective for long-period waves ($10 < T(g/h)^{0.5} < 12$). The interaction of the incident wave with the front wall of OWCs generates a large drop in liquid level at the front sides of chambers far away from the incident direction, which results in better energy conversion for more distant chambers at both short and medium periods. For long-period waves, the large motion and deformation of the breakwater can induce multi-mode scattering waves, which enhance the wave energy conversion of the chambers located at the middle location. Consequently, for commercialized productions such

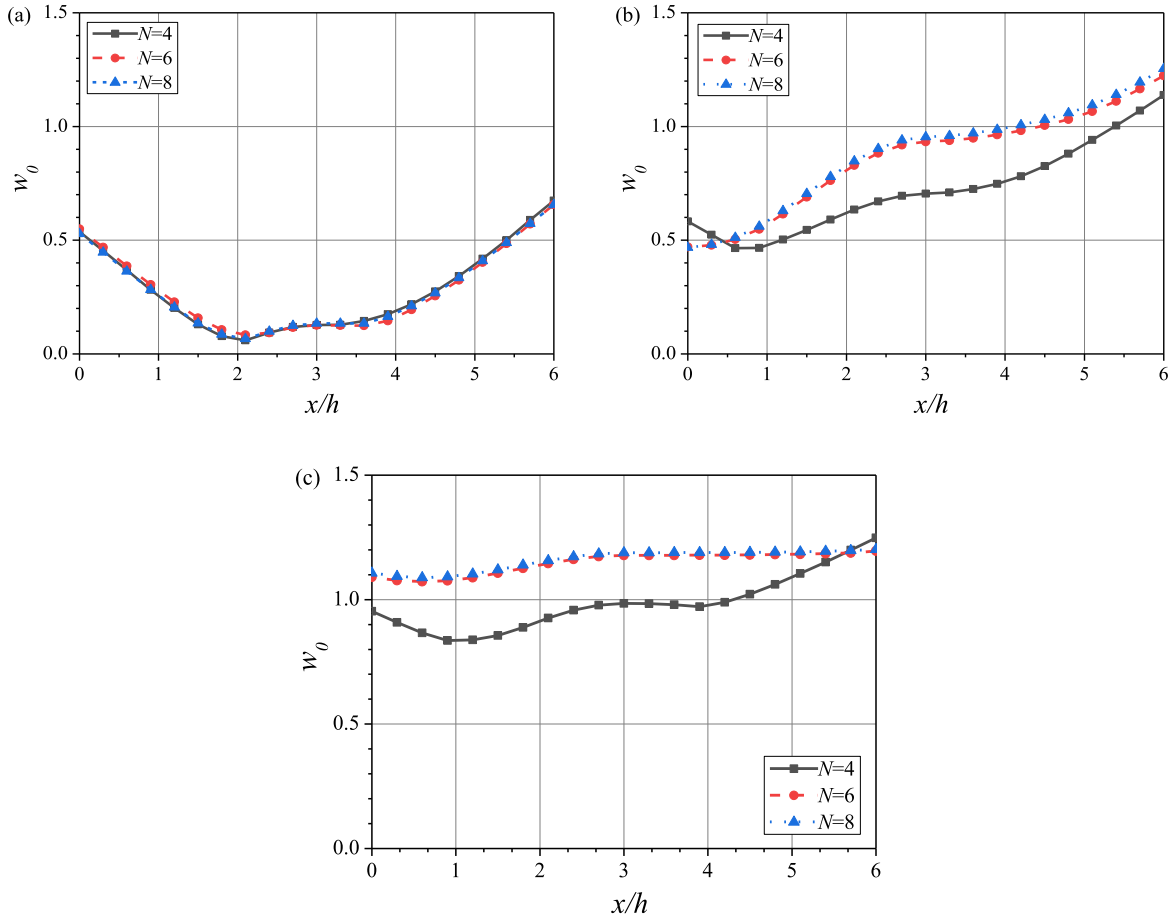

Fig. 10. Deflection amplitude distribution of the flexible floating breakwater along the length direction for different OWC number at (a) $T(g/h)^{0.5} = 4.9$, (b) $T(g/h)^{0.5} = 7.9$ and (c) $T(g/h)^{0.5} = 10.9$.

as wave energy exploitation, more OWC numbers in the along-breakwater direction would be more appropriate, since not only higher energy conversion can be achieved but also a broader applicable range of wave period for the WEC is realized.

To distinguish the wave field around the integrated system, Fig. 9 (a)–(c) shows the spatial dimensionless distribution of wave amplitudes i.e. $2A/H_I$ (A denotes the wave amplitude at arbitrary coordinate) for different OWC numbers. A typical standing wave effect can be observed at the facing-wave sides of chambers, which would harm the structural durability due to the large fluid pressure difference between the wave surfaces outside and inside the chamber. It is also interesting that the wave elevation at different measurement points in each chamber becomes closer to each other as the OWC number increases from $N = 4$ to $N = 8$, which can drive more synchronized pneumatic air movement and lead to higher wave energy extraction as indicated by Fig. 7(b). Additionally, the piston mode motion of the water column in the gap between the OWC and the breakwater is strengthened with increased OWC number, which in turn transferred more waves toward the chambers.

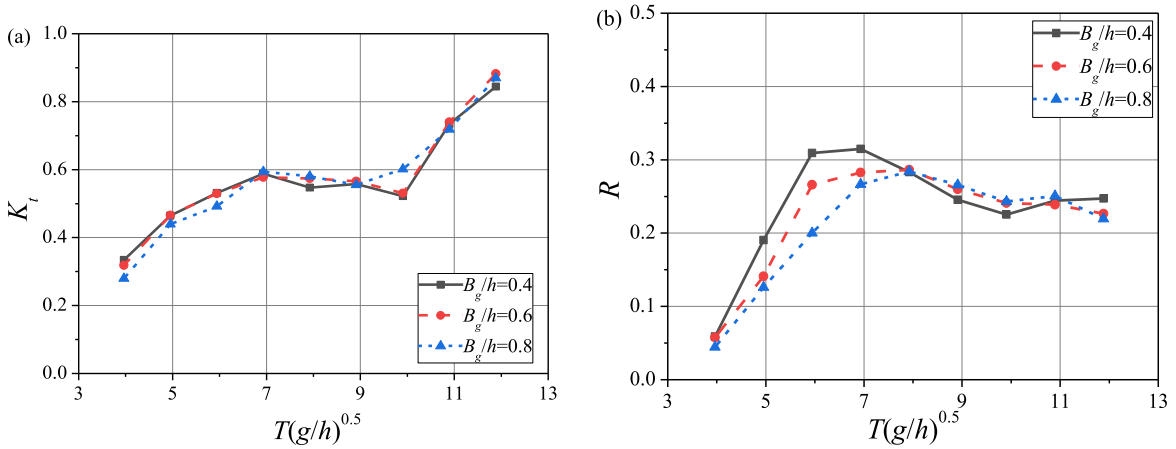

Fig. 11. (a) Transmission coefficient and (b) overall energy conversion efficiency against wave period and breakwater-OWC gap distance.

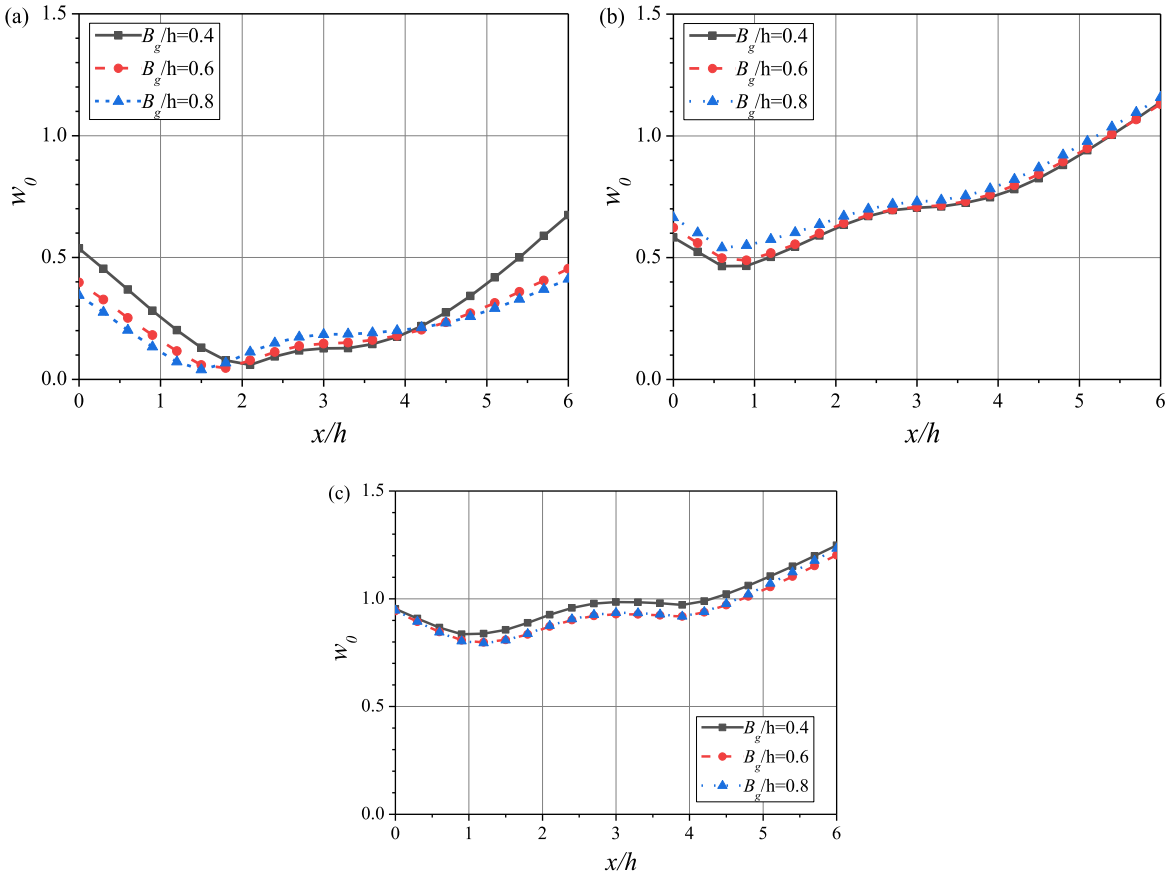

Fig. 12. Deflection amplitude distribution of the flexible floating breakwater along the length direction for different gap distances at (a) $T(g/h)^{0.5} = 4.9$, (b) $T(g/h)^{0.5} = 7.9$ and (c) $T(g/h)^{0.5} = 10.9$.

However, the wave elevation downstream from the breakwater increases with increasing OWC number.

The deflection distribution of the flexible floating breakwater corresponding to different wave periods (i.e. $T(g/h)^{0.5} = 4.9$, 7.9 and 10.9) is plotted in Fig. 10(a)–(c). It is clear, as indicated by Fig. 10(a), that for short-period waves, the deflections at both ends of the breakwater are larger than those at the middle location. This can be explained by the free boundary conditions at the ends, which means that both the bending moment and the shearing stress are negligible at both ends. Moreover, the deflections remain approximately the same for different OWC numbers. This proves that the short-period wave absorption by the array OWC is basically the same for a range of OWC numbers. As N increases to 6 or 8, the hydroelastic response of the breakwater is magnified as shown in Fig. 10(b) and (c), which can be attributed to more transmitted waves over OWCs to fully interact with the breakwater. Fig. 10(c) illustrates that the ratio of the rigid motion and the elastic deflection is gradually reduced with increasing OWC number in long-period waves, which further validates the favourable long-wave attenuation capacity of OWCs with large plane area. Notably, for $N = 4$, the hydroelastic response at the fore-end invariably is smaller than that at the back-end, corresponding to the significant increase of scatting wave elevation in Fig. 9(b).

4.2. Effect of the gap between the floating breakwater and OWCs

To further determine the optimal spacing distance between the floating breakwater and OWCs, three different OWC-breakwater spacing distances, i.e. $B_g/h = 0.4$, 0.6 and 0.8 are considered. The OWC number $N = 4$ is selected and other parameters are the same as in subsection 4.2. Fig. 11(a) and (b) display the variation of the transmission coefficient and the overall energy conversion efficiency against the wave period. As shown in Fig. 11(a), for short-period waves ($T(g/h)^{0.5} < 7$), the transmission coefficient decreases slightly with increasing the spacing distance. This is reasonable as a wider gap can gather more water column mass which is excited by the transmitted waves. A collapse of the transmission coefficient is found at $T(g/h)^{0.5} = 9$ and 10 corresponding to $N = 8$ and 6 (4), due to the wave resonance in the breakwater-OWC gap. This means that the OWC-breakwater gap performs well in the long-wave attenuation, broadening the period range for effective wave-blocking capacity. Fig. 11(b) reveals that the energy conversion efficiency is negatively correlated with the spacing distance in short-period waves, but is positively correlated with long-period waves. In addition, the narrower gap is more beneficial for the peaks of energy conversion efficiency. This is because, for large spacing distance i.e. $B_g/h = 0.8$, short-period transmitted waves intercepted by the breakwater cannot effectively react on the OWC devices, reducing the synergistic effect between the breakwater and the OWCs. However, in long-period waves, the large spacing distance is more favourable for the breakwater to reflect waves into the chambers. At the same time, the location of the maximum energy conversion efficiency shifts toward a higher resonance period in the chamber and the variation becomes more gentle with the spacing distance, which corresponds to $T(g/h)^{0.5} = 6$, 7 and 8 for $B_g/h = 0.4$, 0.6 and 0.8, respectively. This can be attributed to the fact that the waves reflected by the breakwater and the multi-mode waves radiated from the breakwater enter the chamber simultaneously, leading to a phase alteration of waves in the chamber.

Furthermore, Fig. 12(a)–(c) shows the deflection distribution of the flexible breakwater as a function of the B_g/h for short-period waves (i.e. $T(g/h)^{0.5} = 4.9$), medium-period waves (i.e. $T(g/h)^{0.5} = 7.9$) and long-period waves (i.e. $T(g/h)^{0.5} = 10.9$). As indicated by Fig. 12(a), for

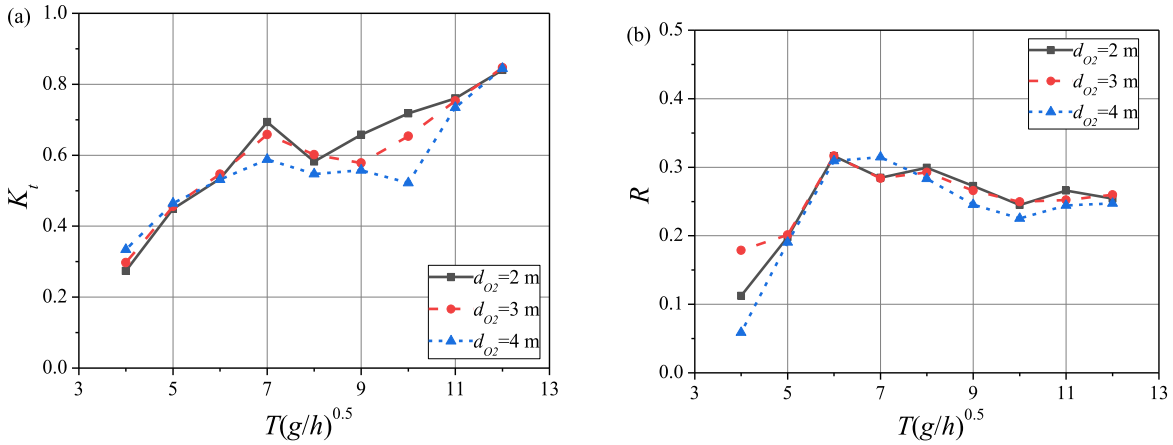

Fig. 13. (a) Transmission coefficient and (b) overall energy conversion efficiency against wave period and sidewall draft of OWCs.

short-period waves, the hydroelastic response at both ends of the breakwater decreases with increasing spacing distance, while it is completely opposite situation for middle parts. This is due to the fact that the shielding effect of the OWCs is weakened with increased spacing distance, where the hydroelastic response of the floating breakwater with a larger spacing distance is more sensitive to oblique waves, inducing an obvious middle arching effect of the flexible structure. For medium-period waves, the total deflection of the floating breakwater monotonically increases with increasing B_g/h as shown in Fig. 12(b), because the higher-order wave components in the OWC-breakwater are reduced with increased spacing distance. As the wave period increases from $T(g/h)^{0.5} = 7.9$ to 10.9, a smaller deflection at the middle location is observed (as indicated by Fig. 12(b) and (c)), suggesting a relatively more constructive interacting effect between OWCs and breakwater.

4.3. Effect of the sidewall draft of OWCs

As mentioned above, the overall energy conversion of OWCs is dependent on the water volume in chambers, which is codetermined by the plane area and the wall draft. So, in this subsection, the hydrodynamic performance of the integrated system is examined with three sidewall drafts of OWCs, i.e. $d_{o2}/h = 0.2$, 0.3 and 0.4. Fig. 13(a) and (b) display the varying trends of the transmission coefficient and the energy conversion efficiency against wave period, respectively. Here, the spacing distance $B_g/h = 0.4$ is selected and other parameters have been fixed to be the same as those set in subsection 4.2. It is worth noting that the present integrated system attenuates transmitted wave height by combining wave energy conversion by OWCs, wave energy dissipation in the OWC-breakwater gap and fluid-structure interaction of the breakwater. Fig. 13(a) shows the slight amplification of the transmission coefficient in short-period waves ($T(g/h)^{0.5} < 5$) with increased sidewall draft of OWCs due to the higher wave reflection from the back OWC chamber wall. However, an opposite trend is observed in medium-period waves ($5 < T(g/h)^{0.5} < 10$), which is a result of more viscous energy dissipation of the water column inside chambers. Besides, the wave periods corresponding to abrupt drop of the transmission coefficient increase with d_{o2}/h, and are $T(g/h)^{0.5} = 8$, 9 and 10 for $d_{o2}/h = 0.2$, 0.3 and 0.4, respectively. This is in accordance with the resonance period $T_w = \sqrt{4\pi^2(d_{o2} + 0.41A_p^2)/g}$ from the OWC, in which T_w is the resonance period of the water column and A_p is the plane area of the chamber. From Fig. 13(b), it is found that the overall efficiency in short-period waves decreases with increased sidewall draft of OWCs and more wave energy transmitted over the integrated system, which coincides well with the variation of the transmission coefficient indicated by Fig. 13(a). Similar variation is also observed in the long-wave range ($T(g/h)^{0.5} > 7$). This is not surprising because the sidewall draft of OWCs changes the wave energy distribution in chambers as illustrated by Fig. 14. For chambers heading toward incident waves, the conversion efficiency is positively correlated with the sidewall draft. A deeper sidewall can more effectively intercept oblique waves, which means that wave propagation can be hindered. Accordingly, the energy conversion performance of chambers far away from the incident waves is weakened. Inversely, the shallower sidewall allows oblique waves to propagate

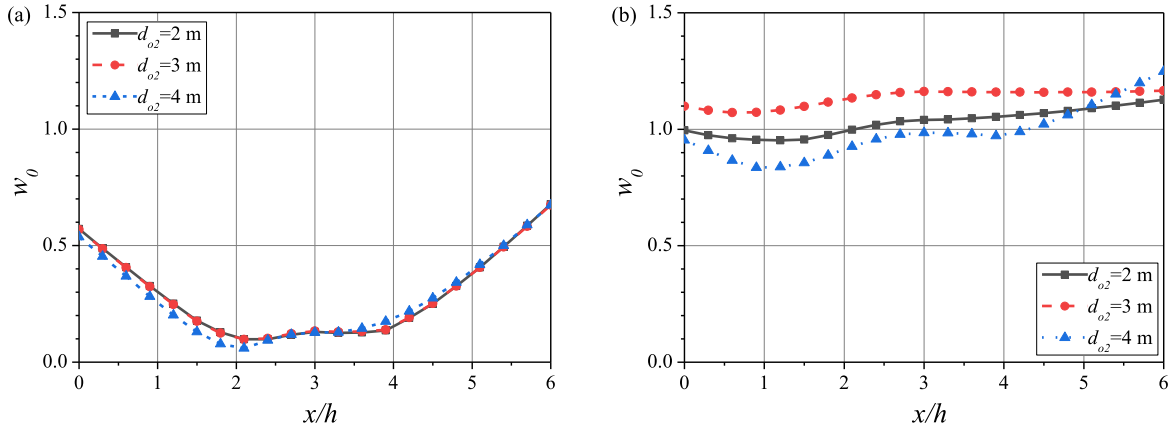

Fig. 14. Deflection amplitude distribution of the flexible floating breakwater along the length direction for different OWC drafts at (a) $T(g/h)^{0.5} = 4.9$ and (b) $T(g/h)^{0.5} = 10.9$.

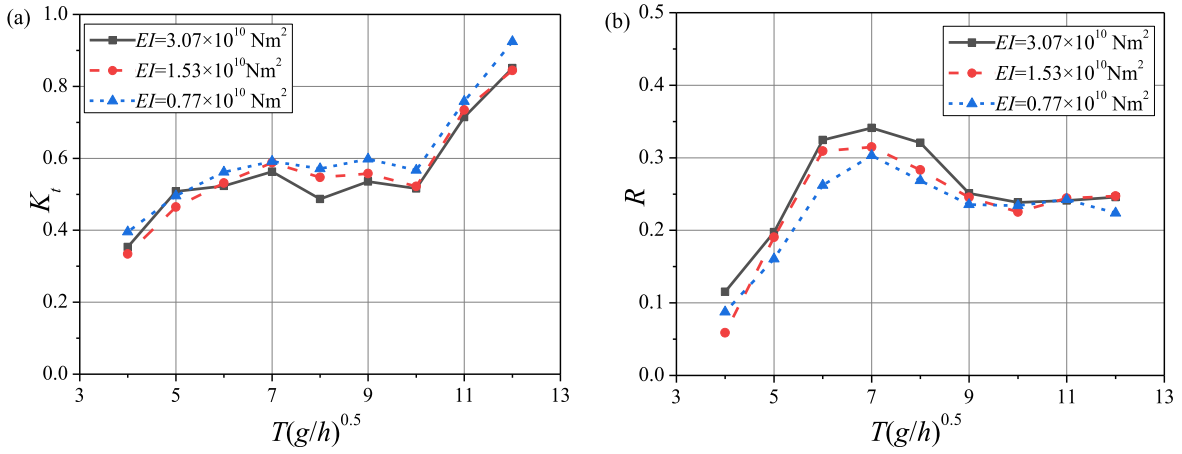

Fig. 15. (a) Transmission coefficient and (b) overall energy conversion efficiency against wave period and breakwater bending stiffness.

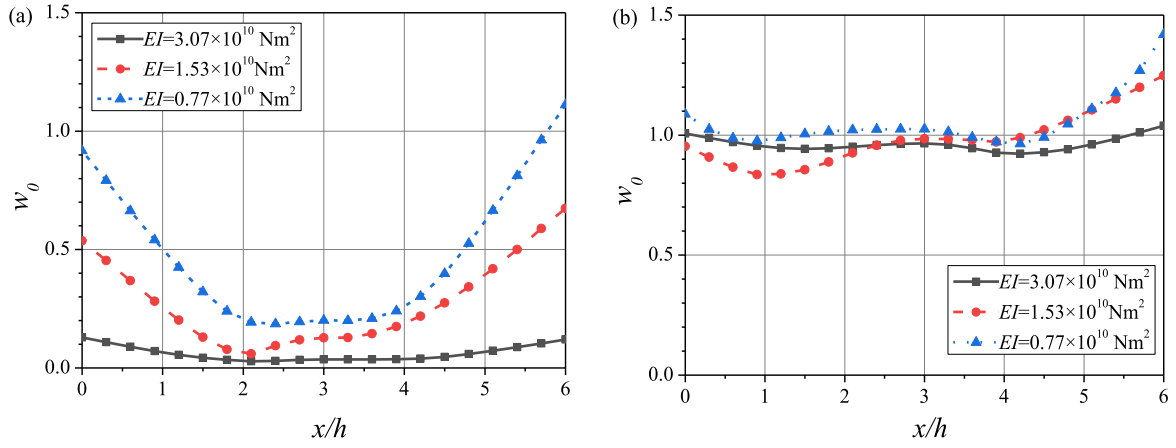

Fig. 16. Deflection amplitude distribution of the flexible floating breakwater along the length direction for breakwater stiffness at (a) $T(g/h)^{0.5} = 4.9$ and (b) $T(g/h)^{0.5} = 10.9$.

with high penetrability, leading to almost identical wave energy conversion among different chambers.

The hydroelastic responses of the flexible breakwater for $T(g/h)^{0.5} = 4.9$ and 10.9 are plotted in Fig. 14(a) and (b), respectively. It is detected from Fig. 14(a) that the curves of the deflection in short-period waves have a slight left shift with increasing sidewall draft of OWCs, suggesting the amplification of the deflection difference between both ends of the breakwater. Specifically, the protection of the breakwater by OWCs with deeper sidewall draft is not uniform along the length direction of the breakwater, which further validates the results in Fig. 12. In Fig. 14(b), for long-period waves, a smaller deflection of the breakwater can be achieved for a deeper sidewall draft. Thus, radiated waves with smaller amplitudes can be generated with the increase of d_{o2}/h, and this shielding effect by the breakwater becomes better which is consistent with the trend of the transmission coefficient as shown in Fig. 13(a).

4.4. Effect of the breakwater stiffness

The heaving motion of the flexible breakwater includes contribution from global heave response due to wave and local elastic deformation due to breakwater elasticity, in which the elastic deformation is strongly dependent on the material properties of the breakwater and this is demonstrated by simulating three bending stiffness of the breakwater, i.e. $EI = 3.07 \times 10^{10}$ Nm^2, 1.53×10^{10} N/m^2 and 0.77×10^{10} N/m^2. Fig. 15(a) and (b) present the influence of the breakwater stiffness on the transmission coefficient and the overall energy conversion efficiency. It is noticed from Fig. 15(a) that the transmission coefficient increases with decreased bending stiffness, especially for medium and long periods ($T(g/h)^{0.5} > 7$), as a result of the significant multi-mode radiated waves generated by the deflections of the flexible breakwater. In other words, the resonant modes of this breakwater are more than one. The basic mode is expected to dovetail nicely with the rigid heaving motion and the higher-order modes are induced by the flexible stiffness. When the flexible stiffness is reduced, more higher-order modes are induced and cause more radiated wave components. The influence of the bending stiffness on the wave energy conversion is opposite to that on the transmission coefficient, as revealed by Fig. 15(b). This is because increased bending stiffness lead to more reflection from the breakwater. Moreover, higher-order radiated waves inside the OWC-breakwater gap may weaken the air flow motion in the chamber because the different interaction among these waves is out of phase.

The hydroelastic distribution of the flexible breakwater in terms of the motion amplitude for $T(g/h)^{0.5} = 4.9$ and 10.9 are given in Fig. 16(a) and (b), respectively. The basic shapes of the deflection curves look like gradually inverted arches with decreasing bending stiffness in short-period waves as seen in Fig. 16(a), which demonstrates that the deflections subjected to oblique waves would be more crucial than the rigid motions for short wave periods. For long-period waves plotted in Fig. 16(b), the overall breakwater structure deflection is much smaller compared with the short-wave period cases because the wave force experienced by different sections of the floating breakwater is relatively smaller.

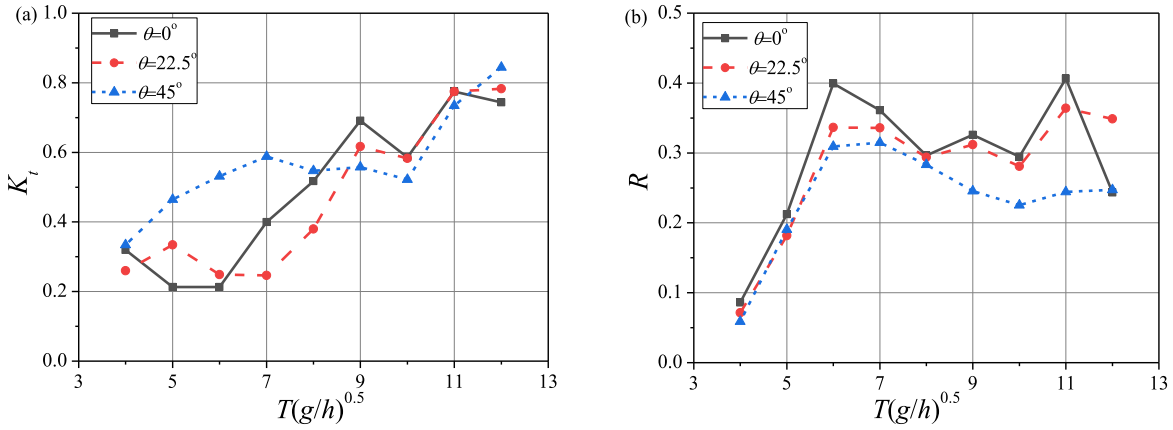

Fig. 17. (a) Transmission coefficient and (b) overall energy conversion efficiency against wave period and breakwater bending stiffness.

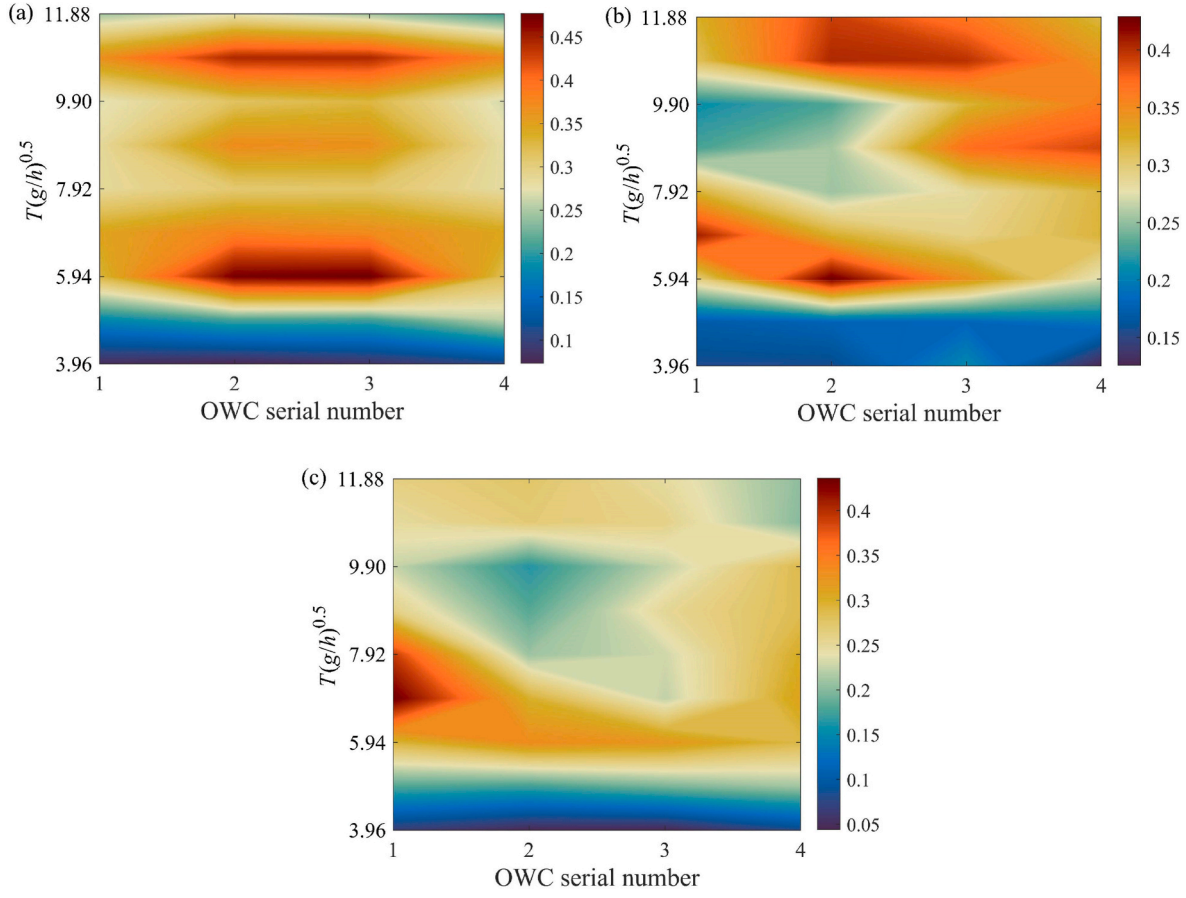

Fig. 18. Efficiency contour for different incident angles i.e. (a) $\theta = 0°$, (b) $\theta = 22.5°$ and (c) $\theta = 45°$.

4.5. *Effect of the incident wave direction*

The above results indicate that the effective wavelength parallel to the breakwater length has a significant effect on the hydroelastic response of the flexible breakwater, further changing the scattering wave field around the integrated system. In this subsection, three different incident wave angles i.e. $\theta = 0°$, 22.5° and 45° are considered. Fig. 17(a) and (b) present the transmission coefficient and the overall energy conversion efficiency of the integrated system for different incident angles. As shown in Fig. 17(a), the transmission coefficient generally increases with increasing incident wave angle in the period range ($5 < T(g/h)^{0.5} < 7$) and vice versa in the long period range ($8 < T(g/h)^{0.5} < 10$). This appears to be caused by the changes in the projected area along the direction normal or parallel to wave propagation. When the heading waves interact with bodies, the integrated system has the maximum projected area normal to the incident direction and provides favourable attenuation performance in short-period waves. As the incident wave angle increases, the effective wavelength normal to the breakwater is reduced and long-wave attenuation is anticipated. It is emphasized that, with the increase of θ, the sudden drop values of the transmission coefficient are reduced, and there is a distinct movement of these values towards a longer wave period. There are three peaks of the efficiency curve observed for small incident wave angles as shown in Fig. 17(b), with the main one around $T(g/h)^{0.5} = 6$, the second at $T(g/$

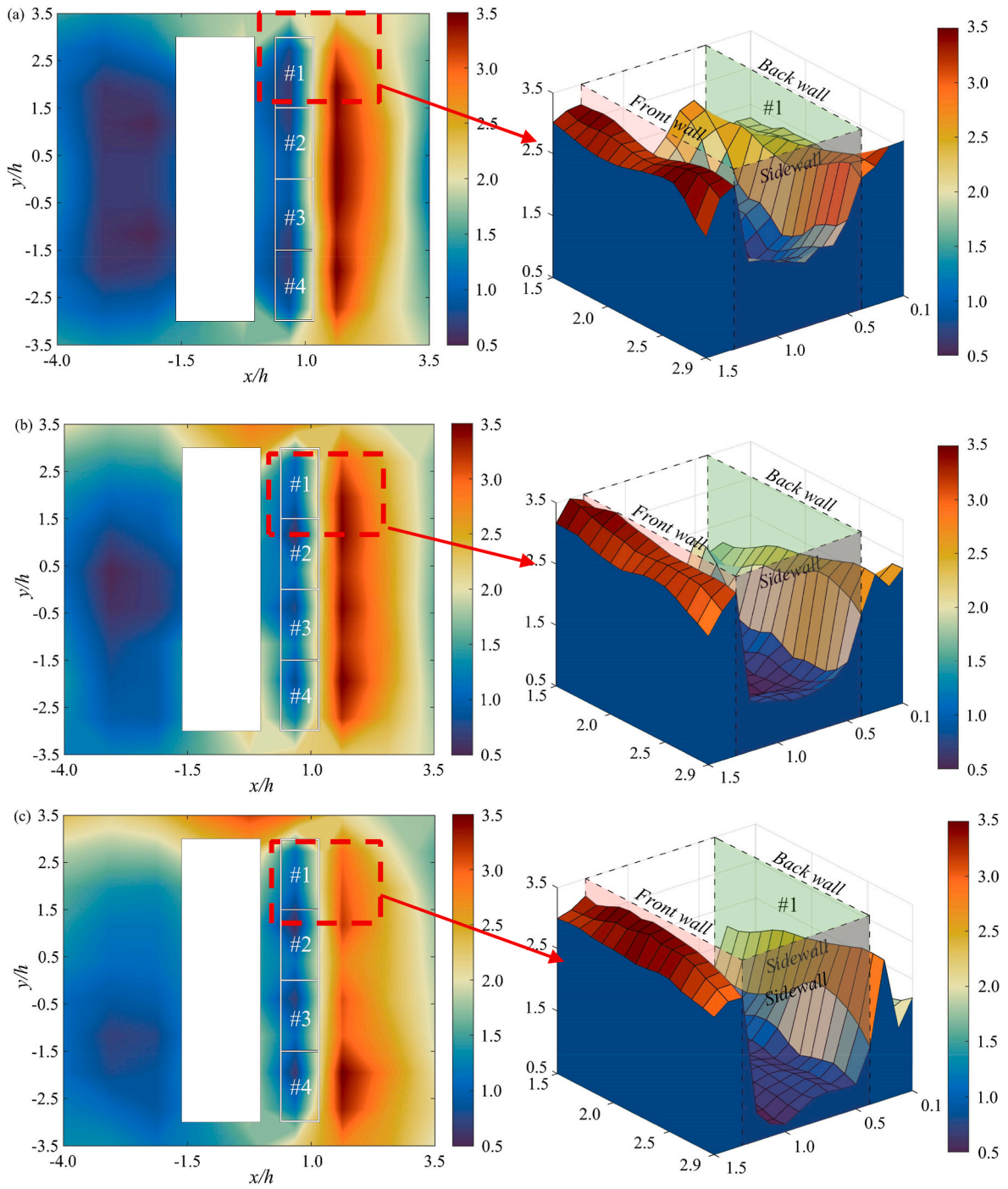

Fig. 19. Wave amplitude distribution around the integrated system for different incident angles i.e. (a) $\theta = 0°$, (b) $\theta = 22.5°$ and (c) $\theta = 45°$.

$h)^{0.5} = 9$ and the third sharp one at long period $T(g/h)^{0.5} = 11$. It also reveals that smaller incident wave angles are more favourable for array OWCs extracting wave energy. This would be associated with the fact that a smaller incident angle enhances the consistency of the liquid level rising and falling within the chamber, which can be further explained by the wave field as shown in Fig. 18 ($T(g/h)^{0.5} = 7.9$). The high consistency of the liquid motion in the chamber can fully utilize the wave absorption effect of the pneumatic damping and compress the air inside the chambers more effectively. Notably, the incident angle changes the wave propagating characteristics. Specifically, stronger reflected wave energy is evenly concentrated at the facing side of OWCs with reduced incident angles, leading to lower wave transmission and a larger shielding effect of the breakwater.

Meanwhile, the efficiency distribution along all chambers for different incident wave angles varies with wave period, as shown in Fig. 18(a)(c). It can be learned from Fig. 18(a) that for headwaves, i.e. $\theta = 0°$, the efficiency of each chamber is more or less similar, and the chambers near the middle location outperform those at the ends, illustrating a constructive array interaction between chambers. Fig. 19(a) shows that the liquid level within the chambers rises and falls with a high degree of uniformity, which allows the OWC device to fully exploit the wave attenuation effect of OWC pneumatic damping and compress the air within the chambers more efficiently. As the incident angle increases to $\theta = 22.5°$ as plotted in Fig. 18(b), the efficiency difference among different chambers becomes more obvious, and the energy conversion performance of OWCs at lee side cannot continuously converter

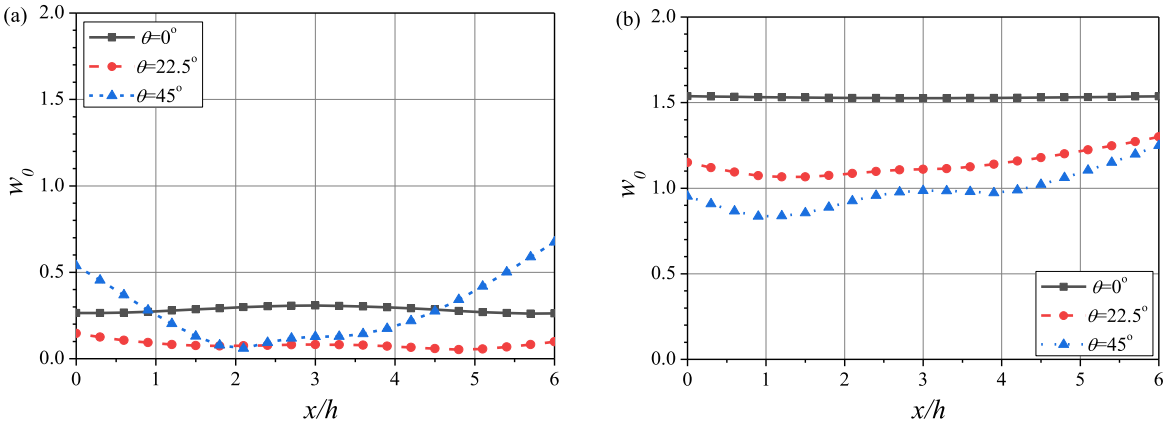

Fig. 20. Deflection amplitude distribution of the flexible floating breakwater along the length direction for incident wave angles at (a) $T(g/h)^{0.5} = 4.9$ and (b) $T(g/h)^{0.5} = 10.9$.

wave energy in a broad range of wave periods. For example, for short-period waves, the chambers closer to the incident direction are more advantageous, whereas for long-period waves, those near the back end of the breakwater perform better. When θ further increases to 45°, the energy conversion sharply decreases. This can be explained by the reflection cause by the breakwater. In the open water domain, the height of undisturbed propagating waves is H_i, but that at the facing-side of the breakwater can reach approximatively a maximum value of $2H_i$ for incident angle $\theta = 0°$ based on the principle of complete reflection. This significantly enhanced the wave energy conversion, simply due to more available wave power. For oblique incident waves, the reflection by the breakwater is weakened due to part of wave propagation along the breakwater length. Also, it can be seen in Fig. 19(b) and (c) that the fluctuation of the liquid level inside the chamber increases with the increasing angle of incidence, but this irregular rise and fall of the liquid level is detrimental to the efficiency of OWCs. Hence, High energy conversion of OWCs benefits from both the constructive array effect and the constructive reflection effect introduced by the breakwater.

Fig. 20(a) and (b) shows the hydroelastic response of the flexible breakwater for $T(g/h)^{0.5} = 4.9$ and 10.9. For incident angle $\theta = 0°$, the breakwater always maintains an obvious rigid motion and small deformation due to uniform wave loads on the wetted body surface. As incident wave angle increases in long-period waves, as shown by Fig. 20 (b), the motion response reduces because of the characteristic length of breakwater along wave propagation direction increases. This leads to response out of phase with waves, and thus wave loads are more uneven, making the role of the deformation in the total response more prominent.

5. Conclusions

Very long floating breakwater systems are more appropriate in practical coastal engineering to provide sufficient shielding areas and protect coastal infrastructures. On the other hand, to accelerate commercialization of WEC devices, an array configuration with efficient wave energy conversion can be implemented onto a very long floating breakwater. In this work, the wave energy absorption by multiple OWCs integrated with a long-flexible floating breakwater is investigated. There exists a narrow gap between OWCs and the breakwater, inducing obvious wave resonance and energy dissipation. Combining CFD and FEM theories, a two-way coupling numerical model is established to solve the hydroelastic problem, which includes the deflections of the flexible breakwater in the simulation. The hydrodynamic mechanisms of the proposed concept, including air-water-solid interaction, rigid-flexible motions and multi-body interferences of the present integrated system, are elaborated. The numerical simulation examed the effect of different designed variables, i.e. OWC number, gap distance, OWC draft, breakwater stiffness and incident wave angle, which can obtain the fundamental rules of both wave energy conversion and wave height attenuation associated with the integrated system. Some valuable conclusions can be summarized as follows

(1) The investigation on the number of OWC devices suggests that a smaller number of larger-plane OWCs are preferred in terms of wave attenuation performance, however, a smaller number of OWCs weakens wave energy conversion. Under the premise of identical dimensions, the one(s) near the end and middle locations have the highest energy conversion in medium-period and long-period waves, respectively.
(2) There is a sudden collapse in the transmission curve with a wave period around the resonant period of water in the OWC-breakwater gap. Water motions in a narrower gap can enhance the maximum energy conversion efficiency when subject to shorter wave period waves.
(3) Both the wave transmission coefficient and the energy conversion decrease with increasing sidewall drafts of OWCs.
(4) Due to the large length-width ratio, the floating breakwater lies on the water surface behaves like a compliant body (hydroelectricity). Simulation results suggest that those multi-mode radiated waves induced by elastic deformations play a destructive role in wave energy attenuation and wave energy conversion for most of the investigated wave periods. However, the reflected waves by the breakwater can boost the excitation energy flux, leading to a higher energy conversion.
(5) The incident wave angle affects water resonances inside the OWC chambers and the OWC-breakwater gap, and therefore affects the wave energy absorption by the integrated system. Specifically, the wave energy distribution is uniform along the array configuration subjected to head waves, whereas that is gradually balanced by individual OWCs with increasing incident angle.

The design of the array WECs integrated with a long floating breakwater can provide a promising way to achieve both marine structural protection and wave energy utilization, helping to guide optimal configuration and commercial operation. For this very long floating integrated system, wave-air-structure interaction is a complex physical problem. The advantages of the present numerical method include the consideration of fluid viscosity, hydroelastic responses and multi-body interferences. The limitation of the present work is the assumption that only the heave motion is considered, and all horizontal motions are restricted numerically. The horizontal motions may have an impact on the wave energy conversion of the integrated system and is

will be included in future study.

When the proposed integrated system is deployed in realistic irregular waves with spread directions, the hydrodynamic behaviour is more complicated due to the coexistence of multiple incident wave frequencies and directions, multiple opening structures and multiple moving modes, which are all coupled to each other. The present CFD-FEM hybrid method can be extended straightforwardly to an in-depth study of this mechanism, which will also be explored in the future as a continuation of this work.

CRediT authorship contribution statement

Yong Cheng: Methodology, Software, Data curation, Writing - original draft, Supervision. **Weiming Du:** Validation, Formal analysis, Writing - original draft, Investigation. **Saishuai Dai:** Formal analysis, Data curation, Writing - review & editing, Supervision. **Zhiming Yuan:** Writing - review & editing. **Atilla Incecik:** Supervision.

Declaration of competing interest

The authors declare that they have no known competing financial interests or personal relationships that could have appeared to influence the work reported in this paper.

Data availability

Data will be made available on request.

Acknowledgements

The authors are grateful to the National Natural Science Foundation of China (Grant No. 52271278, 52111530137), Natural Science Found of Jiangsu Province (Grant No. SBK2022020579) and the Newton Advanced Fellowships (Grant No. NAF\R1\180304) by the Royal Society for supporting this work.

References

[1] IEA. Global energy review: CO2 emissions in 2021. https://www.iea.org/reports/global-energy-review-co2-emissions-in-2021-2, [accessed 21 November 2022].
[2] IREA. Word energy transitions outlook. https://www.irena.org/publications/2022/Mar/World-Energy-Transitions-Outlook-2022. [Accessed 21 November 2022].
[3] Gunn K, Stock-Williams C. Quantifying the global wave power resource. Renew Energy 2012;44:296–304.
[4] Zhao XL, Ning DZ, Zou QP, Qiao DS, Cai SQ. Hybrid floating breakwater-WEC system: a review. Ocean Eng 2019;186:106126.
[5] Tay ZY. Effect of resonance and wave reflection in semi-enclosed moonpool on performance enhancement of point absorber arrays. Ocean Eng 2022;243:110182.
[6] Chen W, Gao F, Meng X, Chen B, Ren A. W2P: a high-power integrated generation unit for offshore wind power and ocean wave energy. Ocean Eng 2016;128:41–7.
[7] Falcão António F de O. Wave energy utilization: a review of the technologies. Renew Sustain Energy Rev 2010;14:899–918.
[8] Vassiliou V, Charalambides M, Menicou M, Chartosia N, Tzen E, Evagelos B, Papadopoulos P, Loucaides A. Aquaculture feed management system powered by renewable energy sources: investment justification. Aquacult Econ Manag 2015;19(4):423–43.
[9] Ning D, Zhao X, Göteman M, Kang H. Hydrodynamic performance of a pile restrained WEC-type floating breakwater: an experimental study. Renew Energy 2016;95:531–41.
[10] Garnaud X, Mei CC. Wave-power extraction by a compact array of buoys. J Fluid Mech 2009;635:389–413.
[11] Ning DZ, Zhao XL, Zhao M, Hann M, Kang HG. Analytical investigation of hydrodynamic performance of a dual pontoon WEC-type breakwater. Appl Ocean Res 2017;65:102–11.
[12] Favaretto C, Martinelli L, Ruol P, Cortellazzo G. Investigation on possible layouts of a catamaran floating breakwater behind a wave energy converter. Proceedings of the 27th international offshore and polar engineering conference. 2017. San Francisco, USA.
[13] Zhao X, Ning D. Experimental investigation of breakwater-type WEC composed of both stationary and floating pontoons. Energy 2018;155:226–33.
[14] Ning D, Zhao X, Zhao M, Kang H. Experimental investigation on hydrodynamic performance of a dual pontoon–power take-off type wave energy converter integrated with floating breakwaters. P I Mech Eng M-J Eng 2018:1475090218804677.
[15] Ouyang H, Chen K, Tsai C. Investigation on bragg reflection of surface water waves induced by a train of fixed floating pontoon breakwaters. Int J Nav Arch Ocean 2015;7(6):951–63.
[16] Madhi F, Yeung RW, Sinclair ME. Energy-capturing floating breakwater. 2015.
[17] Madhi F, Sinclair ME, Yeung RW. The "Berkeley wedge": an asymmetrical energy-capturing floating breakwater of high performance. Mar Syst Ocean Technol 2014;9(1):5–16.
[18] Madhi F, Yeung RW. On survivability of asymmetric wave-energy converters in extreme waves. Renew Energy 2018;119:891–909.
[19] Tay ZY. Performance and wave impact of an integrated multi-raft wave energy converter with floating breakwater for tropical climate. Ocean Eng 2020;218:108136.
[20] Cheng Y, Xi C, Dai S, Ji CY, Collu M, Li MX, Yuan ZM, Incecik A. Wave energy extraction and hydroelastic response reduction of modular floating breakwaters as array wave energy converters integrated into a very large floating structure. Appl Energy 2022;306:117953.
[21] Koo W. Non-linear time–domain analysis of motion-restrained pneumatic floating breakwater. Ocean Eng 2009;36(9):723–31.
[22] Zhao XL, Zhang LD, Li MW, Johanning L. Experimental investigation on the hydrodynamic performance of a multi-chamber OWC-breakwater. Renew Sustain Energy Rev 2021;150:111512.
[23] He F, Huang Z, Law AWK. An experimental study of a floating breakwater with asymmetric pneumatic chambers for wave energy extraction. Appl Energy 2013;106:222–31.
[24] He F, Huang Z. Hydrodynamic performance of pile-supported owc-type structures as breakwaters: an experimental study. Ocean Eng 2014;88:618–26.
[25] Sundar V, Moan T, Hals J. Conceptual design of OWC wave energy converters combined with breakwater structures. ASME 2010 29th international conference on ocean, offshore and arctic engineering. 2010. Shanghai, China.
[26] Malara G, Romolo A, Fiamma V, Arena F. On the modelling of water column oscillations in U-OWC energy harvesters. Renew Energy 2017;101:964–72.
[27] Boccotti P. Comparison between a U-OWC and a conventional OWC. Ocean Eng 2007;34:799–805.
[28] Ning D, Guo B, Wang R, Vyzikas T, Greaves D. Geometrical investigation of a U-shaped oscillating water column wave energy device. Appl Ocean Res 2020;97:102105.
[29] Pecher A, Le Crom I, Kofoed JP, Neumann F, Azevedo E de B. Performance assessment of the Pico OWC power plant following the equimar methodology. PAroceedings of the twenty-first international offshore polar engineering conference. USA: Hawaii; 2011.
[30] Childs JF. The role of converters and their control in the recovery of wave energy. Proceedings of the institution of electrical engineers (IEE) colloquium on power electronics for renewable energy. 1997.
[31] Whittaker TJT, Beattie W, Folley M, Boake C, Wright A, Osterried M. The LIMPET wave power project-the first years of operation. 2004.
[32] Martins-Rivas H, Mei CC. Wave power extraction from an oscillating water column at the tip of a breakwater. J Fluid Mech 2009;626:395–414.
[33] Tsai CP, Ko CH, Chen YC. Investigation on performance of a modified breakwater-integrated OWC wave energy converter. Sustainability 2018;10(3):1–20. https://doi.org/10.3390/su10030643.
[34] Zhou Y, Ning D, Shi W, Johanning L, Liang D. Hydrodynamic investigation on an OWC wave energy converter integrated into an offshore wind turbine monopole. Coast Eng 2020;162:103731.
[35] Zheng S, Antonini A, Zhang Y, Greaves D, Miles J, Iglesias G. Wave power extraction from multiple oscillating water columns along a straight coast. J Fluid Mech 2019;878:445–80.
[36] Elhanafi A, Macfarlane G, Fleming A, Leong Z. Experimental and numerical investigations on the hydrodynamic performance of a floating–moored oscillating water column wave energy converter. Appl Energy 2017;205:369–90.
[37] Marjani AE, Ruiz FC, Rodriguez MA, Santos MTP. Numerical modelling in wave energy conversion systems. Energy 2008;33:1246–53.
[38] Deng Z, Ren X, Wang L, Wang P. Hydrodynamic performance of a noveloscillating-water-column breakwater with a horizontal bottom-plate: experimental and numerical study. Ocean Eng 2019;187:106174.
[39] Elhanafi A, Macfarlane G, Ning DZ. Hydrodynamic performance of single-chamber and dual-chamber offshore-stationary oscillating water column devices using CFD. Appl Energy 2018;228:82–96.
[40] Kuriqi A, Pinheiro AN, Sordo-Ward A, Garrote L. Water-energy-ecosystem nexus: balancing competing interests at a run-of-river hydropower plant coupling a hydrologic-ecohydraulic approach. Energ Convers Manage 2020;223:113267.
[41] Kuriqi A, Jurasz J. Chapter 21- Small hydropower plants proliferation and fluvial ecosystem conservation nexus. Complementarity of variable renewable energy sources. 2022. p. 503–27.
[42] Cheng Y, Fu L, Dai SS, Collu M, Cui L, Yuan ZM, Incecik A. Experimental and numerical analysis of a hybrid WEC-breakwater system combining an oscillating water column and an oscillating buoy. Renew Sustain Energy Rev 2022;169:112909.
[43] Cheng Y, Fu L, Dai SS, Collu M, Ji CY, Yuan ZM, Incecik A. Experimental and numerical investigation of WEC-type floating breakwaters: a single-pontoon oscillating buoy and a dual-pontoon oscillating water column. Coast Eng 2022;177:104188.
[44] Howe D, Nader JR, Macfarlane G. Experimental investigation of multiple oscillating water column wave energy converters integrated in a floating breakwater: energy extraction performance. Appl Ocean Res 2020;97:102086.

[45] Howe D, Nader JR, Macfarlane G. Experimental investigation of multiple oscillating water column wave energy converters integrated in a floating breakwater: energy extraction performance. Appl Ocean Res 2020;99:102160.
[46] Dhavalikar S, Awasare S, Joga R, Kar AR. Whipping response analysis by one way fluid structure interaction-A case study. Ocean Eng 2015;103:10–20.
[47] Takami T, Matsui S, Oka M, Iijima K. A numerical simulation method for predicting global and local hydroelastic response of a ship based on CFD and FEA coupling. Mar Struct 2018;59:368–86.
[48] Lakshmynarayanana PA, Temarel P. Application of CFD and FEA coupling to predict dynamic behaviour of a flexible barge in regular head waves. Mar Struct 2019;65:308–25.
[49] Ferziger J, Peric M. Computational Methods for fluid dynamics. third ed. Springer; 2003.
[50] Bathe KJ, Wilson EL. Numerical methods in finite element analysis. Englewood, NJ: Prentice-Hall; 1976.
[51] Kim Y, Kim J. Benchmark study on motions and loads of a 6750-TEU containership. Ocean Eng 2016;119:262–73.